Article

Mineralogy and Mineral Chemistry of Dioritic Dykes, Quartz Diorite Enclaves and Pyroxene of the Sungun Cu-Mo Porphyry Deposit, East Azerbaijan, Iran

Amin Allah Kamali [1,*], Mohsen Moayyed [2], Benoit M. Saumur [3] and Mohammad Fadaeian [4]

1 Research Center for Conservation of Culture Relics (RCCCR), Research Institute of Cultural Heritage & Tourism, Tehran 11369-13431, Iran
2 Department of Earth Sciences, University of Tabriz, Tabriz 51664-14766, Iran
3 Département des Sciences de la Terre et de l'Atmosphère, Université du Québec à Montréal, 201 Avenue du Président-Kennedy, Case Postale 8888, Succursale Centre-Ville, Montréal, QC H3C 3P8, Canada
4 Department of Geology, Payame Noor University, Tehran 19395-4697, Iran
* Correspondence: aminkamali1984@gmail.com

Abstract: The Sungun Cu-Mo porphyry deposit forms part of the Ahar–Arasbaran Magmatic Belt (AAMB). Its host Miocene porphyry stock is quartz monzonitic in composition and is cut by intermediate dykes that post-date mineralization. These dykes contain pyroxene and enclaves of ambiguous origin. Dykes of microdiorite are observed within quartz diorite dykes, whereas later diorite dykes contain three different kinds of enclaves (diorite, quartz diorite and hornfels) of sizes between 1 and 10 cm. Enclaves consist of plagioclase, hornblende and biotite, with accessory sphene, quartz and apatite. Chlorite compositions in microdiorite are within the chamosite range, whereas they are within the clinochlore range in diorite enclaves. Microprobe analyses of pyroxene indicate an augitic composition (Fs13.38-22.79Wo29.1-33.57En48.53-56.61), consistent with an igneous origin. Hornblende of the diorite enclaves formed at pressures ranging between 3 and 5.3 kilobars and temperatures between 714 and 731 °C. Average oxygen fugacity during rock formation is −14.75. Such high oxygen fugacities suggest that the diorite formed near the boundaries of a convergent margin. Amphibole compositions suggest that the diorite enclaves are sub-alkaline to mildly alkaline, consistent with reported whole-rock chemistry of the Sungun magmas. Pyroxenes were formed at pressures ranging between 11 and 15 kilobars (33–45 km) and temperatures between 1100 and 1400 °C. The amount of Fe^{3+} in clinopyroxene is also consistent with high oxygen fugacity within their environment of crystallization. Overall, these results have implications for our understanding of the origin of the Sungun Cu-Mo porphyry magmas and their mineral deposits in a lower-crustal setting.

Keywords: enclave; amphibole; pyroxene; thermometry–barometry; Sungun

1. Introduction

Porphyry deposits, suppliers of ~75% of the world's copper and significant proportions of Mo, Au and Re, are formed in subduction-related magmatic arcs [1] and, to some extent, in post-subduction collisional zones [2]. They are associated with magmas of intermediate to felsic composition (mostly andesitic to dacitic), having calc-alkaline to alkaline affinity [1]. In modern environments, porphyry-related deposits are usually found within active subduction zones and, in ancient environments, these ores are associated with former collision zones [1,2]. The global distribution of known Cu-Au porphyry deposits shows a clear spatial relationship with volcanic arc terranes at convergent plate margins (e.g., [1,3]). The Sungun Cu-Mo porphyry deposit, which is the focus of this study, was formed in a post-collisional environment [4]. Studies of the Sungun plutonic rocks and deposit, thus, provide the opportunity to document petrological and geochemical controls that affect mineralization in such environments.

The Sungun Cu-Mo deposit, situated 32 km north of the Varzaghan, East Azerbaijan Province, contains ore reserves of 740 Mt at 0.65 % Cu and ~0.01% Mo and is located within the Cenozoic Ahar–Arasbaran Magmatic Belt (AAMB) of northwestern Iran. The AAMB is part of the Alborz-Azerbaijan-Lesser Caucasus Magmatic Belt, which resulted from the subduction and subsequent collision along the southern margin of Eurasia [5] (Figure 1). The Alborz-Azerbaijan belt hosts many world-class porphyry copper deposits, such as Haft Cheshme, Ali Javad, Sieh Kemer Mianeh, Sahibdivan Meshkin Shahr and Sonajil Harris. These deposits are associated with calc-alkaline to shoshonitic stocks and dykes containing rocks exhibiting typical porphyritic textures [4,6,7]. The host Cenozoic volcanic and plutonic rocks of this belt have medium to high K, calc-alkaline to alkaline composition and the deposits show common characteristics regarding their geology, host rocks, ages, alteration and mineralization [8–10]. A notable characteristic of Sungun is the presence of eight generations of dykes that cross-cut the deposit ([11,12] and references therein) and these dykes are genetically linked to the magmatic-hydrothermal system that generated the deposit [4] and, therefore, may provide clues with regards to temperature–pressure conditions in the magmatic plumbing system.
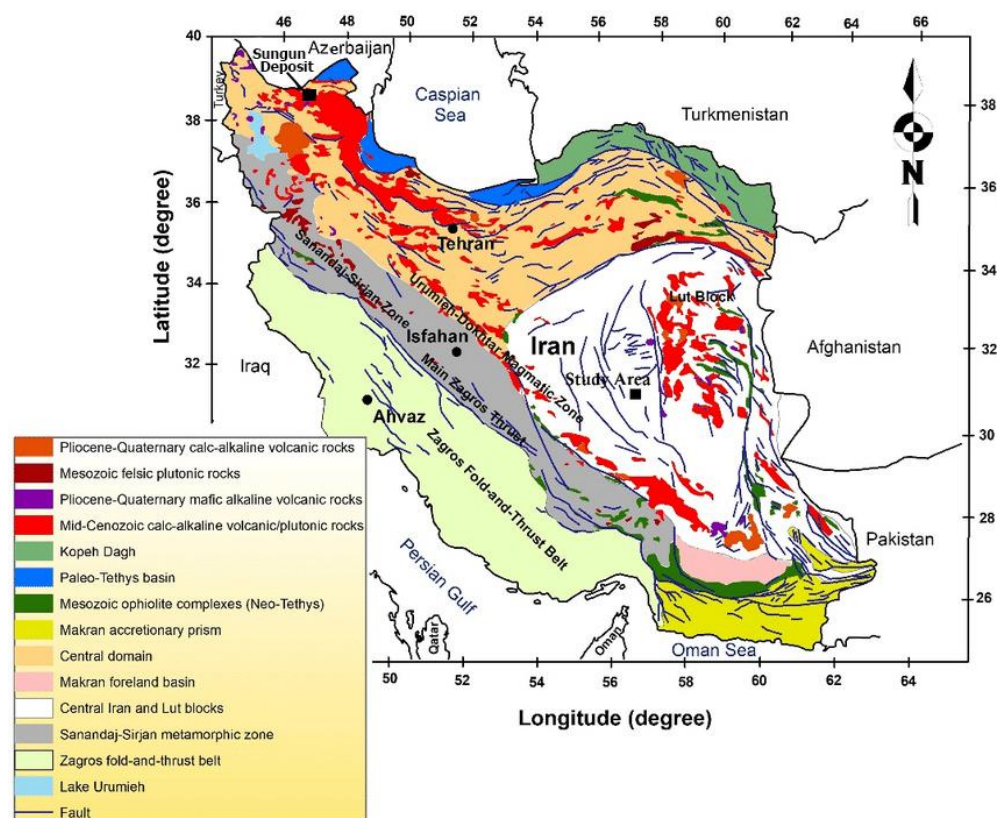
Figure 1. Regional tectonic map of Iran [12] showing the location of the study area.

Among the dyke generations observed at Sungun, diorite dykes ("Pulse 1" of [11]) contain several types of enclaves; these include enclaves of quartz diorite, diorite, microdiorite and hornfels, with the former three sharing mineralogical and geochemical characteristics with their host dykes. Pyroxene also occurs within these dykes, yet is poorly understood from a petrogenic point of view. This paper aims to elucidate the source and genesis of the Sungun enclaves and pyroxene and constrain physical and chemical conditions for their formation, (i.e., pressure, temperature, oxygen fugacity) based on field observations, petrographic features and mineral chemistry. Our results also have implications for our understanding of the genesis of the Sungun deposit, notably with respect to temperatures of alteration and the documentation of a number of magmatic episodes.

2. General Geology

The Oligocene Sungun porphyry has been the subject of several geological and metallogenic studies [4,13,14]. Dated at 20.69 and 21 Ma by Ar-Ar ad U-Pb (SHRIMP), respectively [15], it was emplaced within a 500 m thick sequence of folded upper Cretaceous limestone with intercalations of shale and Eocene volcaniclastic rocks and sandstones [14,16]. Quartz monzonite, which hosts Cu-Mo mineralization, represents the earliest and most voluminous magmatic phase of the Sungun porphyry [17]. The interaction of the Sungun porphyry stock with surrounding Cretaceous limestone produced skarn zones in the northern and eastern periphery of the porphyry; this skarn contains clinopyroxene that was also analyzed in this study. Hornfels are usually observed along the edges of the eastern occurrences of skarn along topographic scars.

Alteration and mineralization are concentric and centered on the Sungun intrusion and interpreted as coeval with its emplacement [8]. Documented hydrothermal alteration consists of an early phase of potassic and propylitic alteration. This early event is associated with the hypogene copper mineralization, precipitated as chalcopyrite and bornite, as both dissemination and veinlets. Molybdenite associated with quartz veins is associated with the early potassic event but located within internal portions of the Sungun intrusion. These events were followed sequentially by phyllic, silicic and argillic stages of alteration.

The initial phase of quartz monzonite magmatism was followed by pulses of diorite and, finally, andesitic magmatism [8,16]. This later activity is associated with the emplacement of multiple generations of dykes within both the voluminous quartz monzonite body and surrounding carbonate country rocks. Rocks exposed at the Sungun Copper Mine include the mineralized Sungun porphyry as well as eight groups of cross-cutting and lithologically distinct post-mineralization dykes(Figure 2). In order of emplacement, these include quartz diorite (DK1a, DK1b, DK1c), diorite (DK3), gabbrodiorite, microdiorite, lamprophyre and dacite [4,11]. Relative ages and cross-cutting relationships were documented during detailed field studies, core logging and the identification of sequences of alteration [11].

Previous geochemical studies show that the Sungun dykes and porphyry have a common origin, with bulk rock compositions more consistent with the post-collisional magmatic arc domain compared to magmas from continental active margins [4,11,14]. However, the dykes are compositionally slightly more mafic than the porphyry. $^{87}Sr/^{86}Sr$ and $^{143}Nd/^{144}Nd$ ratios for the porphyry and dykes, with the exception of microdiorite and lamprophyric dykes, are consistent with a mantle source and closed-system fractionation [4]. At a maximum pressure of 19 kbar, gravitational separation of the magmas within a lower-crustal magmatic chamber gave rise to a dioritic magma. This magma then rose and settled into another chamber at a maximum of 6 kbar (~18 km), where it fractionated and gravitationally separated. These magmas rose again in sequence, thereby creating the more felsic and earlier Sungun porphyry and the subsequent intermediate Sungun dykes [16,18].

Among the eight groups of Sungun dykes discussed earlier, only four of these groups are relevant to this study: from oldest to youngest, these are the DK1a, DK1b and DK1c groups consisting of quartz diorite and DK3 consisting of diorite. Based on age determinations by [9,15], the emplacement age for DK1a ranges between 20.57 and 19.85 Ma. DK1a and DK1b dykes contain microdiorite enclaves as well as DK1b autobreccia (Figure 3a,c). DK1c dykes have been observed in the pit section of boreholes, but it is exhalant in the eastern skarn section of the mine. DK3 dykes contain abundant hornfels enclaves and autoliths (Figure 3e,g).
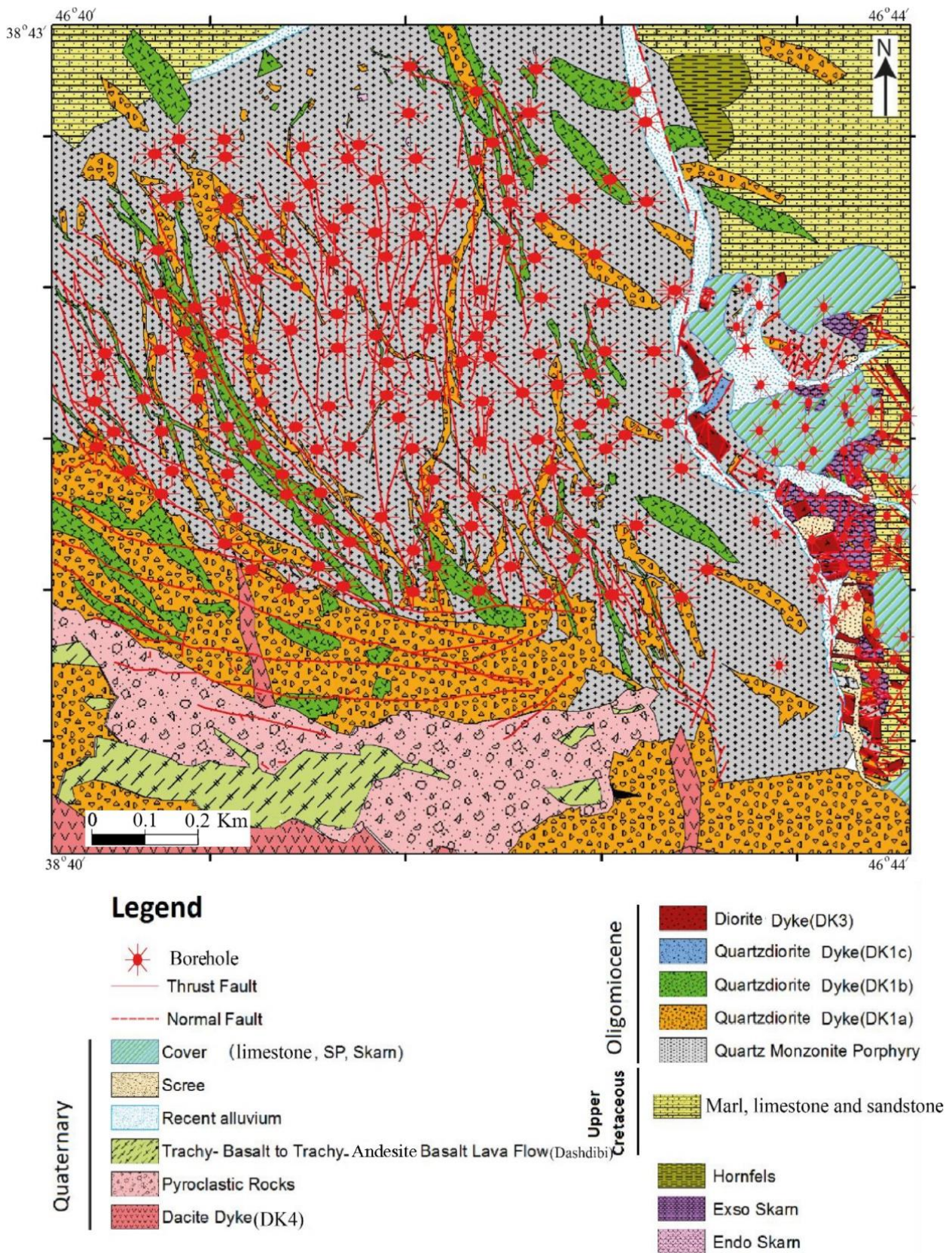
Figure 2. Geological map of the Sungun Copper Mine [11].
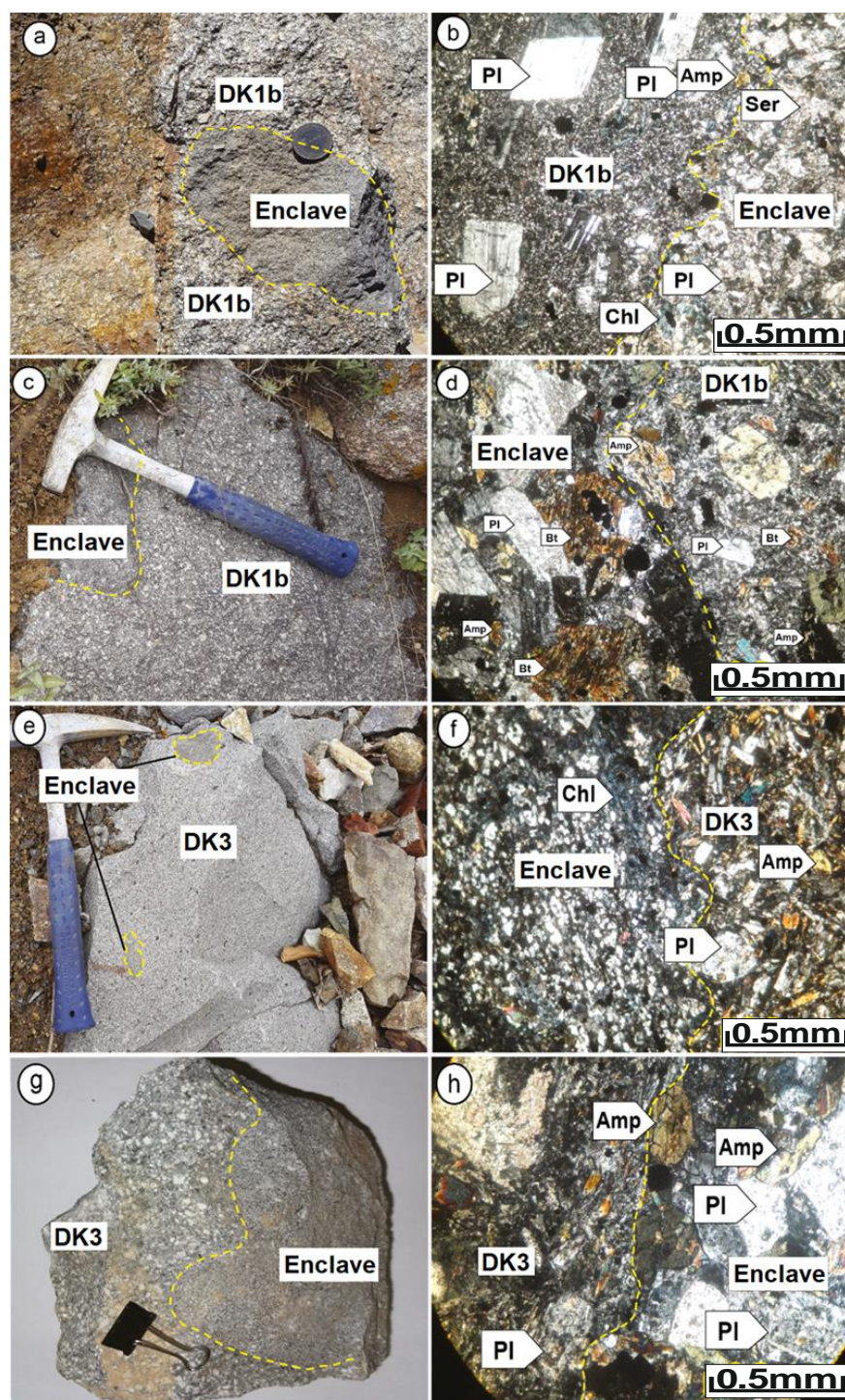
Figure 3. Hand sample (left) and thin section (right) photographs of representative samples from Sungun post-mineralization dykes. All photomicrographs are in plane polarized light. (**a,b**) Microdiorite enclaves in DK1b dykes: (**a**) Mingled contact between a fine-grained microdiorite sheet and a medium-grained quartz diorite. (**b**) Photomicrograph showing the contact between the microdiorite and a quartz diorite. (**c,d**) Quartz diorite enclaves: (**c**) irregular mingled contact between a fine-grained autolith and a medium-grained quartz diorite. (**d**) Boundary between the quartz diorite and its enclave. (**e,f**) Hornfels enclaves in DK3 dykes: (**e**) hornfels xenolith within an outcrop of fine-grained diorite. (**f**) Photomicrograph showing the boundary between the dyke and enclave of hornfels in microscopic scale. (**g,h**) Diorite enclaves in DK3 dykes: (**g**) DK3 xenolith in the dioritic dykes. (**h**) Photomicrograph of the contact of DK3 xenolith with the host diorite dyke.

3. Materials and Methods

Preparation and field operations, sampling and laboratory studies were completed in the autumn and winter of 2013. Petrographic studies were performed using a BX53-P—CX31-P OLYMPUS polarizing microscope Japan Manufacturers.

Geochemical studies of various silicate minerals, such as plagioclase, amphibole, pyroxene and chlorite, were carried out in the laboratory of the Iranian Mineral Research and Technology Center (Imidro) and the Microprobe Laboratory of the University of Oklahoma, USA, using a CAMECA SX100 device, French Cameca company (20 kV, 20 nA, 2 mm spot).

4. Petrography

4.1. Dykes

DK1b dykes (quartz diorite): The main minerals observed in quartz diorite dykes are plagioclase, biotite and amphibole. Plagioclase shows swinging zoning and polysynthetic twins and crystal rims exhibit sericite alteration (Figure 3b). Amphibole is observed as fine- to coarse-grained subhedral to euhedral crystals. Biotite has a weak to strong alteration and, in some cases, has been completely sericitized and chloritized. Dk1b dykes can contain enclaves of microdiorite, which are described in the following section.

DK3 dykes (diorite): These dark green diorites contain unaltered white plagioclase phenocrysts and amphibole (Figure 4a) and exhibit a microlithic porphyritic to coarsely porphyritic texture (Figure 4f). Crystal sizes vary from fine to coarse, plagioclase is subhedral and locally contains sieve texture and swinging zoning (Figure 4b). Amphiboles are subhedral to euhedral and are locally replaced by chlorite, epidote and sericite (Figure 4d), which, in order, represent a typical alteration sequence. Orthoclase, quartz, sphene, apatite and opaque minerals are minor constituents. Diorite dykes can contain large clinopyroxene (augite). These occur as coarse, subhedral to euhedral crystals and in some microscopic sections, augite crystals exhibit exsolution features (Figure 4e,f). DK3 dykes may also contain large enclaves of hornfels and diorite, described below.

4.2. Enclaves

Microdiorite enclaves in DK1b dykes: Enclaves of microdiorite are porphyritic to microlithic, often gray in color in hand sample and are mesocratic to melanocratic. The diameter of these enclaves ranges between 2 and 10 centimeters (Figure 3a). Plagioclase and ferromagnesian minerals form the bulk of the mineralogy. Plagioclase occurs as euhedral to subhedral phenocrysts with polysynthetic twinning and is often moderately to strongly altered to saussurite (Figure 3b). Such crystals form 30–40 modal % of the rock. Ferromagnesian minerals do not occur as phenocrysts and have been completely chloritized (Figure 3b). The fine-grained matrix forms 40%–50% of the rock, but its primary mineralogy is not recognizable due to extreme alteration.

Diorite enclaves in DK3 dykes: These enclaves show the same overall mineralogy as the host DK3 diorite dykes. Hand samples of these enclaves are often dark gray, have sizes ranging between 2 and 7 centimeters and show granular textures (Figure 3g). Plagioclase often occurs as medium to coarse, subhedral to euhedral crystals that have been chlorite and epidote alteration (Figure 3h). Apatite, quartz, sphene and opaques are accessory minerals.

DK1b enclaves in DK3 dykes: Quartz diorite enclaves are granular textured, exhibit sizes ranging between 3 and 10 centimeters (Figure 3d) and hand samples are often gray in color. Chilled contacts of these enclaves with quartz diorite (DK1b) are clearly visible. The main minerals include plagioclase, amphibole and biotite. Plagioclase is observed as euhedral to subhedral, medium- to coarse-grained crystals, has polysynthetic twinning, exhibits poikilitic texture and has moderate alteration. It forms a cumulate phase in some samples, forming up to 65 modal % of one particular enclave (Figure 3d). Amphibole (25–35% modal) is observed as fine to coarse, euhedral to subhedral crystals, exhibiting simple twinning and is only moderately altered. This mineral forms 25–35% of this type of

the enclave and has moderate alteration (Figure 3d). Biotite (10%) is observed as medium to coarse crystals, is euhedral to subhedral and locally forms coronae around poikilitic plagioclase (Figure 3d). Apatite and quartz are accessory phases.

Hornfels enclaves in DK3 dykes: Hand samples of hornfels enclaves are gray, very hard and dense. The size of these enclaves ranges from a few millimeters up to about 5 centimeters (Figure 3f). They are fine grained and contain quartz, hornblende, epidote, chlorite, plagioclase and opaque minerals. Epidotized plagioclase and hornblende were also chloritized (Figure 3f). Mineral assemblages are consistent with metamorphism in the Hornblende Hornfels facies.
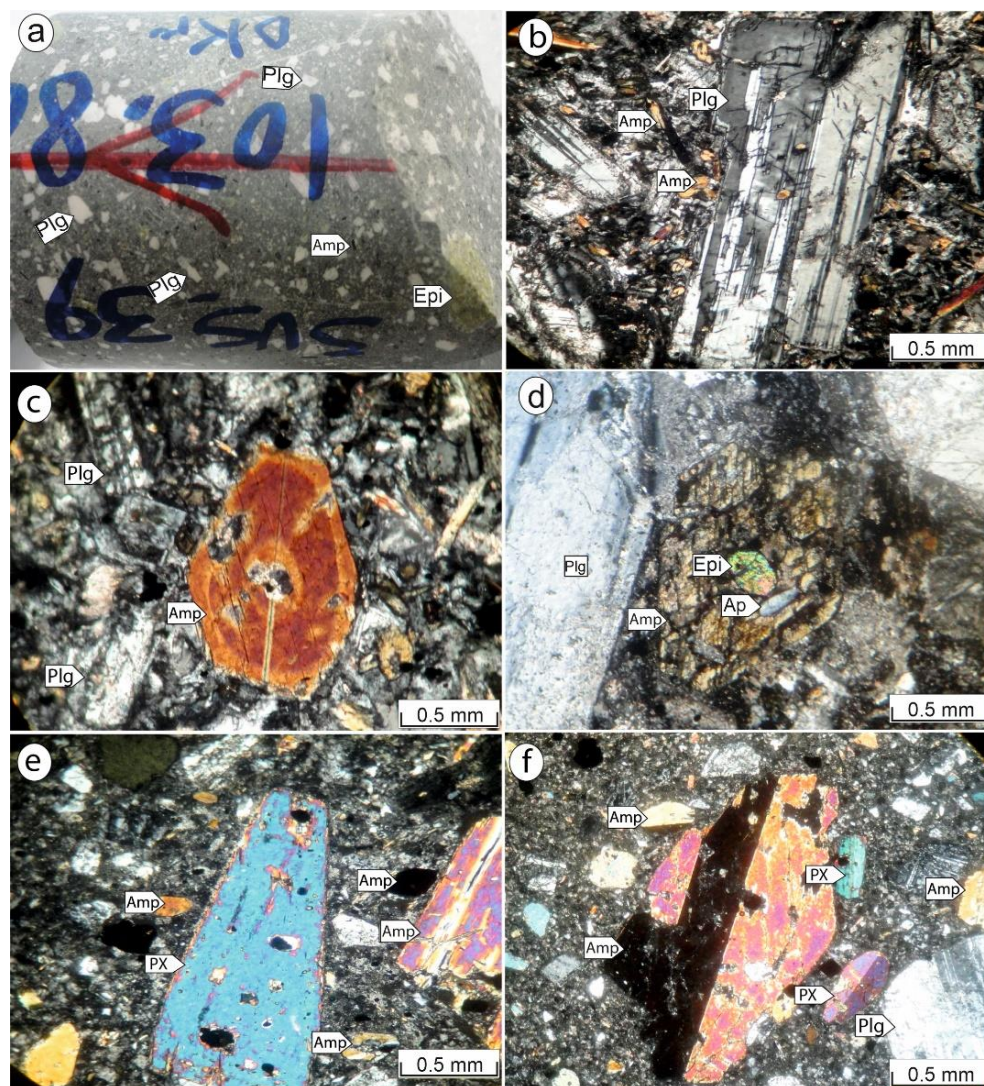
Figure 4. (**a**) A hand specimen from the dioritic dykes (coarse plagioclase (plg), epidote (Epi) and amphibole (Amp)); (**b**) plagioclase phenocrysts exhibiting twinning; (**c**) euhedral amphiboles and plagioclase. (**d**) Alteration in amphibole and plagioclase in diorite dykes; (**e**,**f**) pyroxene in diorite dykes (DK3).

5. Mineral Chemistry of Microdiorite and Diorite Enclaves

5.1. Plagioclase Chemistry

The results of EPMA of plagioclase are shown in Table 1, based on five cations and eight oxygen atoms. In all samples, plagioclase is highly sodic albite, although some slightly calcic grains from microdiorite enclaves plot as oligoclase (Figure 5). The An content for plagioclase from microdiorite enclaves varies between 2.73% and 15.07% and

that for the diorite enclaves between 2.88% and 4.89%. Average values are 7.89% and 3.82%, respectively. The composition of plagioclase in the quartz diorite dykes (DK1a, DK1b and DK1c) varies from albite-oligoclase to andesine and oligoclase to andesine; in the diorite, it varies from andesine to labradorite; in the LAM, from albite to oligoclase; and in the microdiorite (MDI), it occurs as albite [11].
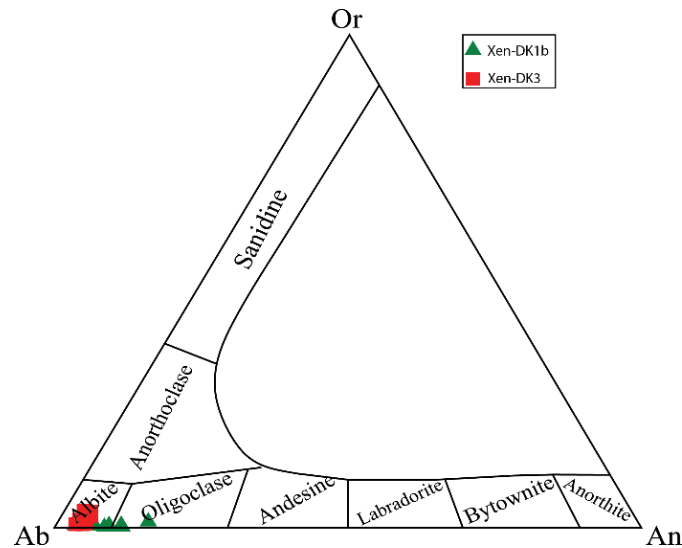
Figure 5. Plagioclase phenocryst compositions for each of the diorite and microdiorite enclaves [19].

5.2. Chlorite Chemistry

Chemical analyses of chlorite, together with the calculated unit cell formulae, are presented in Table 2 (based on 14 oxygen atoms) and compositions are plotted in Figure 6. In the $Fe/(Mg + Fe^{2+}) - Al^{IV}/(Si + Al^{IV})$ diagram, chlorite of microdiorite and diorite enclaves is located in the aluminum Al-chamosite and Al-Fe clinochlore, respectively (Figure 6a). Further, in the $Si - Mg/(Mg + Fe)$ diagram, which isolates clinochlore and chamozite endmember compositions, diorite and microdioritic enclaves are, respectively, located within the clinochlore and chamozite (Figure 6b).The chemical composition of the chlorite in the quartz diorite (DK1a and DK1b), diorite (DK3) and MDI dykes falls in the range of the pycnochlorite field and, in the dyke DK1c, it is within the pennine field [11].
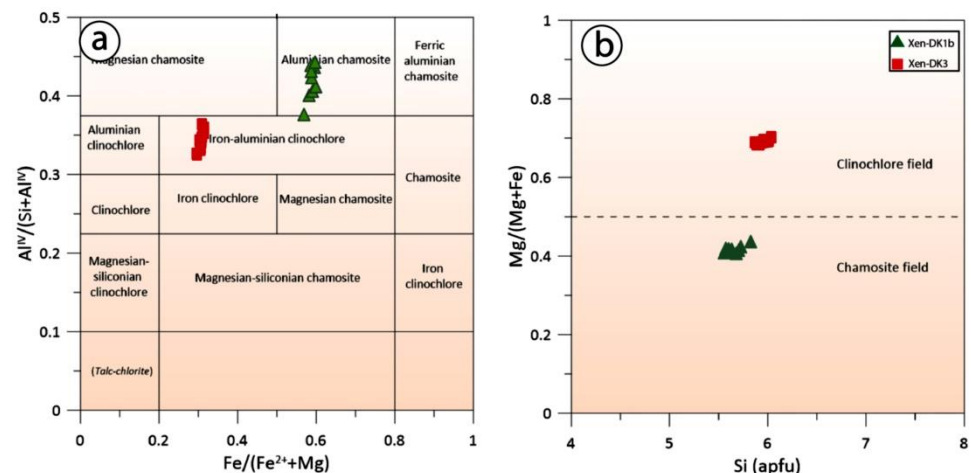
Figure 6. Compositional variations of chlorites in terms of (**a**) $Fe/(Mg+Fe^{2+})$ versus $AlIV/(Si+Al^{IV})$ [20]. (**b**) $Mg/(Mg+Fe)$ versus Si [21] from diorite and microdiorite enclaves (cations/28 oxygen atoms).

Table 1. Representative analyses of plagioclase from diorite and micro diorite enclaves.

Sample	Xen-DK1b									Xen-DK3								
	Pl1	Pl2	Pl3	Pl4	b1	b2	b3	b4	b5	K1	K2	K3	K4	K5	K6	K7	K8	K9
SiO_2	67.28	65.11	66	66.76	64.14	66.06	67.41	67.46	66.87	67.35	66.44	67.62	66.78	66.43	66.82	67.26	64.11	67.33
TiO_2	0.02	0	0.03	0	0	0.03	0.01	0	0	0	0	0.02	0.05	0.05	0.02	0.02	0.08	0.03
Al_2O_3	20.65	21.47	21.37	20.73	22.03	20.53	20.18	20.04	21.21	20.31	20.56	19.96	20	20.17	20.25	19.91	20.35	20.28
FeO	0.04	0.03	0.03	0.03	0.09	0.04	0.03	0.02	0.05	0.33	0.39	0.35	0.3	0.36	0.4	0.13	2.92	0.23
MnO	0	0.01	0.02	0.01	0	0.02	0	0	0.01	0.03	0.02	0.03	0.01	0	0.02	0	0.05	0.02
MgO	0	0	0.01	0.01	0.02	0.01	0	0	0.01	0	0.01	0	0	0	0.04	0	0.64	0.08
CaO	1.32	2.32	1.82	1.71	3.18	1.32	0.85	0.58	1.82	0.61	0.83	0.61	0.63	0.97	0.98	0.7	0.86	0.87
Na_2O	10.71	10.32	10.48	10.69	9.74	10.69	11.01	11.32	10.44	10.69	9.99	11.18	10.93	10.89	10.21	10.47	10.87	10.93
K_2O	0.15	0.09	0.07	0.08	0.25	0.1	0.12	0.1	0.13	0.63	0.58	0.17	0.32	0.2	0.42	0.19	0.15	0.38
Total	100.17	99.35	99.82	100.02	99.45	98.81	99.62	99.54	100.53	99.96	98.82	99.94	99.02	99.07	99.16	98.68	100.03	100.15
Formula 8 (O)																		
Si	2.94	2.88	2.9	2.93	2.85	2.93	2.96	2.96	2.92	2.96	2.94	2.96	2.96	2.94	2.95	2.97	2.86	2.95
Ti	0	0	0	0	0	0	0	0	0	0	0	0	0	0	0	0	0	0
Al	1.06	1.12	1.11	1.07	1.15	1.07	1.04	1.04	1.09	1.05	1.07	1.03	1.04	1.05	1.05	1.04	1.07	1.05
Fe^{2+}	0	0	0	0	0	0	0	0	0	0.01	0.01	0.01	0.01	0.01	0.01	0	0.11	0.01
Mn	0	0	0	0	0	0	0	0	0	0	0	0	0	0	0	0	0	0
Mg	0	0	0	0	0	0	0	0	0	0	0	0	0	0	0	0	0.04	0.01
Ca	0.06	0.11	0.09	0.08	0.15	0.06	0.04	0.03	0.08	0.03	0.04	0.03	0.03	0.05	0.05	0.03	0.04	0.04
Na	0.91	0.89	0.89	0.91	0.84	0.92	0.94	0.96	0.88	0.91	0.86	0.95	0.94	0.94	0.87	0.9	0.94	0.93
K	0.01	0	0	0	0.01	0.01	0.01	0.01	0.01	0.04	0.03	0.01	0.02	0.01	0.02	0.01	0.01	0.02
Total	4.98	5	4.99	4.99	5	5	4.99	5	4.98	4.99	4.97	5	5	5	4.97	4.96	5.08	5
Ab	92.86	88.52	90.88	91.48	83.51	93.07	95.22	96.67	90.57	93.43	92.2	96.16	95.13	94.22	92.59	95.35	94.97	93.72
Or	0.84	0.48	0.41	0.46	1.42	0.59	0.69	0.59	0.72	3.64	3.54	0.96	1.86	1.14	2.52	1.13	0.87	2.14
An	6.3	11	8.71	8.07	15.07	6.34	4.08	2.74	8.71	2.93	4.26	2.88	3.01	4.64	4.89	3.52	4.16	4.14

Table 2. Representative major-element compositions of chlorite from studied diorite and microdiorite enclaves.

	Xen-DK1b										Xen-DK3														
Sample	b1	b2	b3	b4	b5	b6	b7	b8	b9	b10	k1	k2	k3	k4	k5	k6	k7	k8	k9	k10	k11	k12	k13	k14	k15
SiO_2	25.43	26.45	26.25	26.30	26.14	26.06	25.61	27.01	25.90	25.59	29.41	29.20	29.42	29.20	28.95	28.97	29.05	29.07	28.48	28.95	28.67	30.15	29.00	28.91	28.75
TiO_2	0.04	0.04	0.01	0.03	0.07	0.09	0.02	0.05	0.03	0.08	0.01	0.02	0.00	0.03	0.01	0.01	0.01	0.02	0.02	0.01	0.00	0.02	0.00	0.02	0.01
Al_2O_3	19.14	18.67	18.53	18.82	18.83	19.12	19.27	17.85	19.39	19.68	18.59	18.69	18.57	18.60	18.85	18.13	17.83	18.20	18.26	17.73	18.02	18.23	17.34	18.83	18.66
FeO	30.21	29.93	30.46	31.02	30.67	30.26	30.11	29.73	30.15	30.32	16.84	16.87	16.62	17.03	17.32	16.74	16.67	16.63	16.97	16.50	16.69	16.57	16.09	17.16	17.04
MnO	0.58	0.54	0.54	0.58	0.57	0.58	0.56	0.52	0.56	0.59	0.46	0.46	0.43	0.52	0.51	0.49	0.49	0.49	0.50	0.47	0.48	0.48	0.50	0.47	0.47
MgO	11.48	12.03	11.80	11.63	11.49	11.85	11.88	12.60	11.84	11.44	21.28	21.15	21.33	21.22	21.12	21.04	21.10	21.40	20.69	20.98	20.94	22.11	21.35	21.46	20.98
CaO	0.06	0.08	0.18	0.06	0.07	0.12	0.13	0.14	0.10	0.07	0.16	0.14	0.15	0.15	0.15	0.15	0.14	0.12	0.10	0.15	0.17	0.17	0.15	0.15	0.14
K_2O	0.00	0.01	0.01	0.01	0.00	0.01	0.00	0.01	0.01	0.00	0.02	0.01	0.01	0.01	0.01	0.01	0.01	0.00	0.01	0.01	0.02	0.02	0.01	0.01	0.02
F	0.00	0.00	0.00	0.00	0.06	0.00	0.03	0.00	0.00	0.14	0.09	0.04	0.24	0.17	0.07	0.17	0.04	0.09	0.18	0.11	0.26	0.35	0.03	0.12	0.03
Cl	0.01	0.00	0.01	0.01	0.01	0.00	0.01	0.00	0.01	0.01	0.00	0.00	0.00	0.01	0.00	0.00	0.00	0.00	0.01	0.01	0.01	0.00	0.00	0.01	0.00
O=F	0.00	0.00	0.00	0.00	0.03	0.00	0.01	0.00	0.00	0.06	0.04	0.02	0.10	0.07	0.03	0.07	0.02	0.04	0.08	0.05	0.11	0.15	0.01	0.05	0.01
O=Cl	0.00	0.00	0.00	0.00	0.00	0.00	0.00	0.00	0.00	0.00	0.00	0.00	0.00	0.00	0.00	0.00	0.00	0.00	0.00	0.00	0.00	0.00	0.00	0.00	0.00
Total	86.95	87.75	87.79	88.46	87.88	88.09	87.61	87.91	87.99	87.86	86.82	86.56	86.67	86.87	86.96	85.64	85.32	85.98	85.14	84.87	85.15	87.95	84.46	87.09	86.09
											14(O)														
Si	2.79	2.86	2.85	2.84	2.84	2.81	2.78	2.91	2.80	2.78	2.98	2.97	2.99	2.97	2.94	2.98	3.00	2.98	2.96	3.00	2.97	3.02	3.02	2.93	2.95
Ti	0.00	0.00	0.00	0.00	0.01	0.01	0.00	0.00	0.00	0.01	0.00	0.00	0.00	0.00	0.00	0.00	0.00	0.00	0.00	0.00	0.00	0.00	0.00	0.00	0.00
Al	2.47	2.38	2.37	2.39	2.41	2.43	2.47	2.27	2.47	2.52	2.22	2.24	2.22	2.23	2.26	2.20	2.17	2.20	2.23	2.17	2.20	2.15	2.13	2.25	2.25
Fe(2+)	2.77	2.71	2.76	2.80	2.78	2.73	2.74	2.68	2.72	2.75	1.43	1.43	1.41	1.45	1.47	1.44	1.44	1.42	1.47	1.43	1.45	1.39	1.40	1.46	1.46
Mn	0.05	0.05	0.05	0.05	0.05	0.05	0.05	0.05	0.05	0.05	0.04	0.04	0.04	0.04	0.04	0.04	0.04	0.04	0.04	0.04	0.04	0.04	0.04	0.04	0.04
Mg	1.88	1.94	1.91	1.87	1.86	1.91	1.92	2.02	1.91	1.85	3.22	3.21	3.23	3.21	3.20	3.23	3.25	3.27	3.20	3.25	3.24	3.30	3.31	3.24	3.21
Ca	0.01	0.01	0.02	0.01	0.01	0.01	0.02	0.02	0.01	0.01	0.02	0.02	0.02	0.02	0.02	0.02	0.02	0.01	0.01	0.02	0.02	0.02	0.02	0.02	0.02
K	0.00	0.00	0.00	0.00	0.00	0.00	0.00	0.00	0.00	0.00	0.00	0.00	0.00	0.00	0.00	0.00	0.00	0.00	0.00	0.00	0.00	0.00	0.00	0.00	0.00
F	0.00	0.00	0.00	0.00	0.02	0.00	0.01	0.00	0.00	0.05	0.03	0.01	0.08	0.06	0.02	0.06	0.01	0.03	0.06	0.04	0.09	0.11	0.01	0.04	0.01
Cl	0.00	0.00	0.00	0.00	0.00	0.00	0.00	0.00	0.00	0.00	0.00	0.00	0.00	0.00	0.00	0.00	0.00	0.00	0.00	0.00	0.00	0.00	0.00	0.00	0.00
Al(IV)	1.21	1.14	1.15	1.16	1.16	1.19	1.22	1.09	1.20	1.22	1.02	1.03	1.01	1.03	1.06	1.02	1.00	1.02	1.04	1.00	1.03	0.98	0.98	1.07	1.05
Al(VI)	1.26	1.24	1.22	1.23	1.25	1.25	1.25	1.18	1.27	1.29	1.20	1.21	1.21	1.19	1.20	1.18	1.17	1.17	1.19	1.17	1.18	1.16	1.14	1.18	1.20

5.3. Amphibole Chemistry

Amphibole is one of the most abundant and important minerals in the dioritic enclaves of the region. In this study, their chemical composition is calculated based on 13 and 23 cations (Table 3). The studied amphiboles from enclaves, based on the diagram of [22], are located in the calcic group based on (Na + K) > 0.5, Ca > 1.5 and Ti < 0.5, as well as within the sub-group of magnesiohornblende (Figure 7a). Figure 7b shows Ti changes in relation to Al^{IV} for amphibole that have less than 0.5 Ti atoms in their structural formula. In this diagram, amounts of Al^{IV} and Ti are reduced in the structural formula because of high Si contents. In vector diagrams of edenite, pargasite and hornblende substitution, analyzed samples show evidence for hornblende–pargasite replacement (Figure 7c). The amphibole in the Sungun dykes is a combination of hornblende–Tschermakite and ferroTschermakite [11].

Table 3. Representative major-element compositions of amphibole from studied diorite enclave.

Sample	X1	X2	X3	X4	X5	X6	X7	X8	X9	X10
SiO_2	43.16	45.19	45.20	46.15	46.41	44.63	45.26	46.06	44.38	45.36
TiO_2	2.10	1.81	1.84	1.52	1.62	1.72	1.69	1.57	1.83	1.61
Al_2O_3	10.13	8.79	8.63	7.57	7.45	9.07	8.76	8.29	9.19	8.39
FeO	12.95	12.38	12.23	11.72	11.44	12.54	12.48	12.49	12.80	12.47
MnO	0.34	0.36	0.42	0.33	0.30	0.35	0.32	0.33	0.36	0.34
MgO	14.03	15.17	15.09	15.68	16.08	14.84	14.98	15.39	14.21	15.01
CaO	10.83	10.78	10.79	10.68	10.76	10.69	10.71	10.72	10.88	10.64
Na_2O	1.85	1.70	1.66	1.48	1.55	1.75	1.66	1.62	1.71	1.58
K_2O	0.62	0.53	0.54	0.45	0.46	0.58	0.58	0.53	0.61	0.57
Total	98.07	98.80	98.48	97.65	98.16	98.25	98.52	99.10	98.03	98.04
					T					
Si	6.28	6.49	6.51	6.68	6.67	6.45	6.52	6.59	6.46	6.57
Al	1.72	1.49	1.47	1.29	1.26	1.55	1.48	1.40	1.54	1.43
Ti	0.00	0.03	0.02	0.03	0.07	0.01	0.00	0.02	0.00	0.00
Total	8.00	8.00	8.00	8.00	8.00	8.00	8.00	8.00	8.00	8.00
					C					
Al	0.01	0.00	0.00	0.00	0.00	0.00	0.01	0.00	0.03	0.00
Ti	0.23	0.17	0.18	0.13	0.11	0.18	0.18	0.15	0.20	0.17
Fe^{3+}	1.43	1.38	1.33	1.27	1.29	1.40	1.33	1.34	1.29	1.32
Mg	3.04	3.25	3.24	3.38	3.45	3.20	3.22	3.28	3.08	3.24
Fe^{2+}	0.15	0.11	0.15	0.14	0.08	0.12	0.18	0.15	0.27	0.19
Mn^{2+}	0.04	0.04	0.05	0.04	0.04	0.04	0.04	0.04	0.04	0.04
Total	4.90	4.95	4.95	4.97	4.96	4.94	4.95	4.96	4.92	4.96
					B					
Ca	1.69	1.66	1.67	1.66	1.66	1.66	1.65	1.64	1.70	1.65
Na	0.31	0.34	0.33	0.35	0.34	0.35	0.35	0.36	0.30	0.35
Total	2.00	2.00	2.00	2.00	2.00	2.00	2.00	2.00	2.00	2.00
					A					
Na	0.21	0.13	0.13	0.07	0.09	0.15	0.12	0.09	0.18	0.09
K	0.12	0.10	0.10	0.08	0.08	0.11	0.11	0.10	0.11	0.11
Total	0.33	0.23	0.23	0.15	0.17	0.25	0.22	0.19	0.29	0.20

The chemical composition of amphibole is a proxy for the oxygen fugacity of the magma from which it crystallized. Oxygen fugacity can be calculated based on models by [23,24] and according to cationic Fe# ratios. Values between 0 and 0.6 indicate high oxygen fugacity, 0.6 and 0.8 indicates average oxygen fugacity and ratios ~1 indicate low oxygen fugacity. The chemical composition of studied amphibole shows Fe# ratios between 0.28 and 0.33, consistent with high-oxygen-fugacity conditions. An additional oxygen fugacity model [25] was used, using the equation Log fO2 = −30930/T + 14.98 + 0.142 (P − 1)/T. Values ranging

between -15 and -13 for diorite enclaves (Table 6) are, once again, consistent with high oxygen fugacity. Furthermore, the occurrence of quartz and sphene together with amphibole is indicative of high-oxygen-fugacity conditions [25] and, thus, consistent with our calculations.
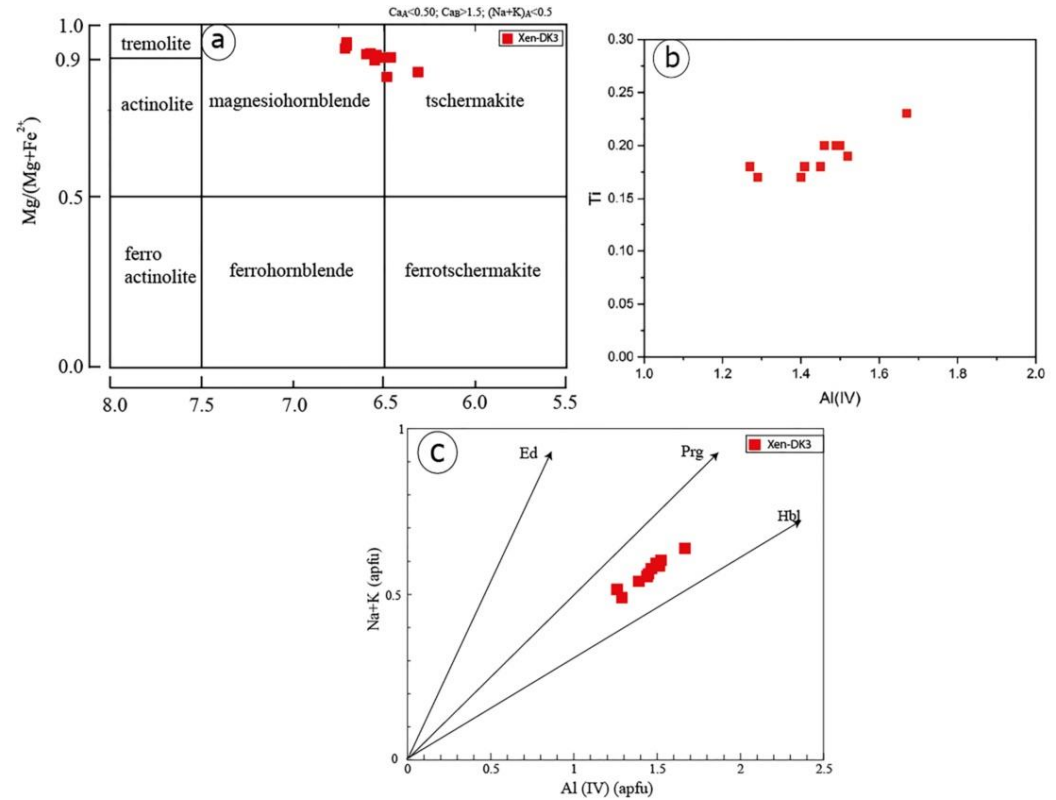
Figure 7. (**a**) Major-element data for amphiboles from diorite enclaves plotted on the Mg/(Mg+Fe^{2+}) vs. Si classification diagram [22]. (**b**) Al (Al^{IV}) plotted vs. Ti for amphibole from the diorite enclaves [22]. (**c**) Exchange vectors diagram of Edenite–Pargazite and Hornblende based on Al^{IV} amounts vs. (Na+K) for diorite enclaves [22].

6. Mineral Chemistry of Pyroxene

This section focuses on clinopyroxene, observed as in DK3-type diorite dykes and a metasomatic phase in Sungun skarn units. The general formula for pyroxene group minerals is M1M2T2O6; the M2 site can be occupied by Ca (Calcic Pyroxenes), Na (sodic pyroxenes), Mn, Fe^{2+} and/or Mg; the M1 position can be occupied by Al, Cr, Fe^{3+}, Ti, Fe^{2+} and/or Mg; and the T position is occupied by Si and Al (e.g., [19]). Structural formulae are calculated based on six oxygen atoms and four cations. The results of the analysis are shown in Table 4. The amount of Al in T site is so elevated that it can compensate the Si^{4+} shortage in the T position. The amounts of Al^{IV} and Si the T site are 0.14–0.27 and 1.73–1.86, respectively. The M1 position frequently has amounts of Mg (0.62–0.80), Fe^{3+} (0.05–0.22), Al^{IV} (0.10–0.16) and Ti (0.03–0.05) and the M2 position is occupied by Ca (0.44–0.51), although others contain Fe^{2+} (0.20–0.33), Mg (0.05–0.18), Na (0.08–0.13), K (0.02–0.05) and Mn (0.01). The observed differences in Fe^{3+} can be described by various modes of oxidation during magmatic conditions. The average composition is as follows:

$(Ca_{0.467}Fe^{2+}_{0.24}Mg_{0.136}Na_{0.108}K_{0.033}Mn_{0.01})(Mg_{0.675}Fe^{3+}_{0.168}Al^{VI}_{0.117}Ti_{0.041})(Si_{1.774}Al^{IV}_{0.225})_2O_6$
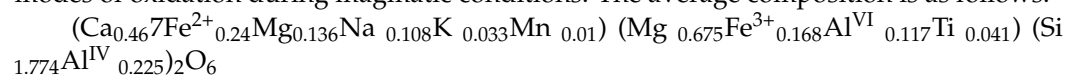
Table 4. EPMA analysis results of pyroxene of diorite dyke and Sungun skarn [26] (chemical composition of pyroxenes and structural formula based on 6 oxygen atoms).

Sample	Sungun										DK3								
point	1	2	3	4	5	6	7	8	9	10	2	3	4	5	6	7	8	9	10
SiO_2	51.15	51.66	51.53	52.31	51.89	52.17	51.35	51.03	51.55	51.64	47.99	46.68	46.55	49.96	47.41	48.38	47.28	47.52	46.32
TiO_2	0.07	0.03	0.13	0.08	0.07	0.02	0.08	0.02	0.12	0.08	1.25	1.62	1.68	1.14	1.22	1.27	1.57	1.68	1.31
Al_2O_3	0.57	0.59	0.63	0.28	0.14	0.13	0.27	0.47	0.64	0.27	7.84	8.31	7.9	5.9	8.03	7.3	8.14	7.78	8.85
Cr_2O_3	0	0	0	0	0	0	0	0	0	0	0	0	0	0	0	0	0	0	0
FeO	14.31	12.93	14.39	13.44	14.24	13.82	14.93	13.67	14.39	14.63	13.53	14.06	12.95	12.1	13.38	12.65	13.16	12.84	13.77
MnO	0.06	0.26	0.08	0.37	0.13	0.06	0.17	0.16	0.09	0.26	0.3	0.36	0.35	0.47	0.44	0.37	0.37	0.38	0.34
MgO	9.08	10.24	9.24	10.74	9.26	9.68	8.69	9.44	9.24	8.96	13.36	12.72	13.65	16.19	15.27	15.73	15.14	15.28	13.51
CaO	23.61	23.59	23.54	22.66	23.77	23.63	23.57	23.28	23.54	23.71	11.81	11.98	12.58	11.23	11.26	11.31	11.21	11.6	12.12
Na_2O	0.98	0.61	0.57	0.54	0.44	0.48	0.58	0.08	0.52	0.33	1.41	1.76	1.56	1.14	1.65	1.59	1.66	1.4	1.56
K_2O	0	0	0	0	0	0	0.04	0.02	0	0	0.86	1.01	0.84	0.39	0.57	0.5	0.64	0.59	0.94
Total	99.83	99.91	100.11	100.42	99.94	99.99	99.68	98.17	100.09	99.88	98.35	98.5	98.06	98.52	99.23	99.1	99.17	99.07	98.72
Si (T)	1.96	1.97	1.97	1.98	1.99	1.99	1.98	1.99	1.97	1.99	1.81	1.76	1.75	1.86	1.75	1.79	1.75	1.77	1.73
Al (T)	0.03	0.03	0.03	0.01	0.01	0.01	0.01	0.01	0.03	0.01	0.19	0.24	0.25	0.14	0.25	0.21	0.25	0.23	0.27
Fe^{3+} (T)	0.02	0.01	0	0.01	0	0	0.01	0	0	0	0	0	0	0	0	0	0	0	0
Total (T)	2	2	2	2	2	2	2	2	2	2	2	2	2	2	2	2	2	2	2
Al (M1)	0	0	0	0	0	0	0	0.01	0	0	0.16	0.13	0.1	0.12	0.1	0.11	0.11	0.11	0.12
Fe^{3+} (M1)	0.11	0.08	0.06	0.05	0.04	0.04	0.06	0	0.06	0.03	0.11	0.2	0.2	0.05	0.21	0.17	0.2	0.16	0.22
Ti (M1)	0	0	0	0	0	0	0	0	0	0	0.04	0.05	0.05	0.03	0.03	0.04	0.04	0.05	0.04
Cr (M1)	0	0	0	0	0	0	0	0	0	0	0	0	0	0	0	0	0	0	0
Mg (M1)	0.52	0.58	0.53	0.61	0.53	0.55	0.5	0.55	0.53	0.51	0.7	0.63	0.65	0.8	0.65	0.69	0.65	0.69	0.62
Fe^{2+} (M1)	0.33	0.33	0.4	0.34	0.42	0.4	0.41	0.44	0.4	0.44	0	0	0	0	0	0	0	0	0
Mn (M1)	0	0.01	0	0	0	0	0.01	0	0	0.01	0	0	0	0	0	0	0	0	0
Total (M1)	0.96	0.99	0.99	1	0.99	1	0.98	1	1	1	1	1	1	1	1	1	1	1	1
Mg (M2)	0	0	0	0	0	0	0	0	0	0	0.05	0.08	0.12	0.11	0.2	0.18	0.19	0.16	0.14
Fe^{2+} (M2)	0	0	0	0.03	0	0	0	0.01	0	0	0.32	0.24	0.21	0.33	0.2	0.22	0.21	0.24	0.21
Mn (M2)	0	0	0	0.01	0	0	0	0.01	0	0	0.01	0.01	0.01	0.01	0.01	0.01	0.01	0.01	0.01
Ca (M2)	0.97	0.96	0.96	0.92	0.98	0.97	0.97	0.97	0.97	0.98	0.48	0.48	0.51	0.45	0.45	0.45	0.44	0.46	0.49
Na (M2)	0.07	0.05	0.04	0.04	0.03	0.04	0.04	0.01	0.04	0.02	0.1	0.13	0.11	0.08	0.12	0.11	0.12	0.1	0.11
K (M2)	0	0	0	0	0	0	0	0	0	0	0.04	0.05	0.04	0.02	0.03	0.02	0.03	0.03	0.04
Total (M2)	1.04	1.01	1.01	1	1.01	1	1.02	1	1	1	1	1	1	1	1	1	1	1	1
Wo	53.38	51.46	51.1	48.59	50.8	50.36	51.62	49.34	50.9	50.6	30.83	33.53	34.2	26.73	30	29.1	29.9	29.88	33.57
En	28.56	31.08	27.91	32.04	27.54	28.7	26.48	27.84	27.8	26.61	48.53	49.53	51.63	53.62	56.61	56.31	56.19	54.77	52.06
Fs	18.06	17.46	21	19.37	21.66	20.94	21.91	22.82	21.31	22.79	20.64	16.94	14.17	19.64	13.38	14.59	13.92	15.34	14.37
Q	1.81	1.87	1.89	1.89	1.92	1.92	1.89	1.97	1.9	1.93	1.55	1.44	1.48	1.68	1.49	1.54	1.49	1.54	1.45
J	0.15	0.09	0.08	0.08	0.07	0.07	0.09	0.01	0.08	0.05	0.21	0.26	0.23	0.17	0.24	0.23	0.24	0.2	0.23

Al and Ti are Tschermak replacement, meaning replacement of Mg and Fe by Ti at the M2 site and replacement of Al by Si at the T site. Accordingly, Al/Ti ratios are greater than 10 (Figure 8a) and the observed correlation between Fe^{3+} and Al (Figure 8b) indicates that the calcium Tschermak component is the most important part of the clinopyroxene's composition. Furthermore, a diagram of Ti-Al^{IV} shows positive correlation that indicates a linked increase between the two elements (Figure 8c). In contrast, samples below the 1:2 line indicate that Al is located in a tetrahedral position to offset other substitutions. The Ti-Mg diagram shows a negative correlation and justifies increases in Ti through replacement of Mg (Figure 8d).
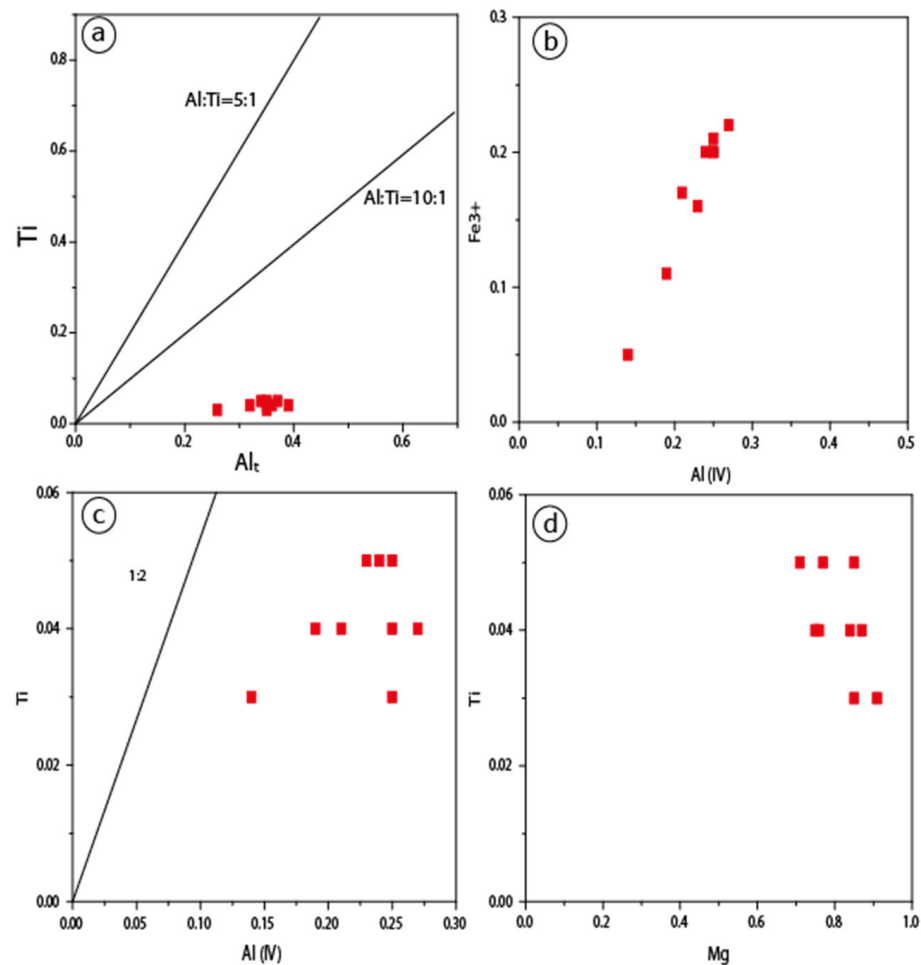
Figure 8. Pyroxene xenolith compositions (**a**) Ti vs. Al diagram, in which most samples are located in the Al/Ti zone > 10, (**b**) Fe^{3+} vs. Al^{IV} diagram where a strong linear correlation between these two cations is observed. (**c**) Ti vs. Al^{IV} diagram, showing a broad positive correlation between the two, (**d**) Ti vs. Mg diagram showing a negative correlation, revealing the increase in Ti at the expense of Mg.

Diagrams of Ti + Cr + Na vs. Al are used to determine whether clinopyroxene is igneous or metamorphic in nature. All analyzed areas have compositions consistent with an igneous origin (Figure 9a). The classification based on the Q-J diagram [27] indicates that crystals are in the group of Ca-Mg-Fe clinopyroxene (Figure 9b). Based on the En-Wo-Fs ternary diagram, clinopyroxene are augite, whereas from the Sungun skarn, are diopside [26] (Figure 9c). In the alternate classification scheme by [28], the Ti-Na-Al^{IV} clinopyroxene ternary diagram shows that clinopyroxene plots in the CATS range, consistent with clinopyroxene Tschermak calcium compositions (Figure 9d).
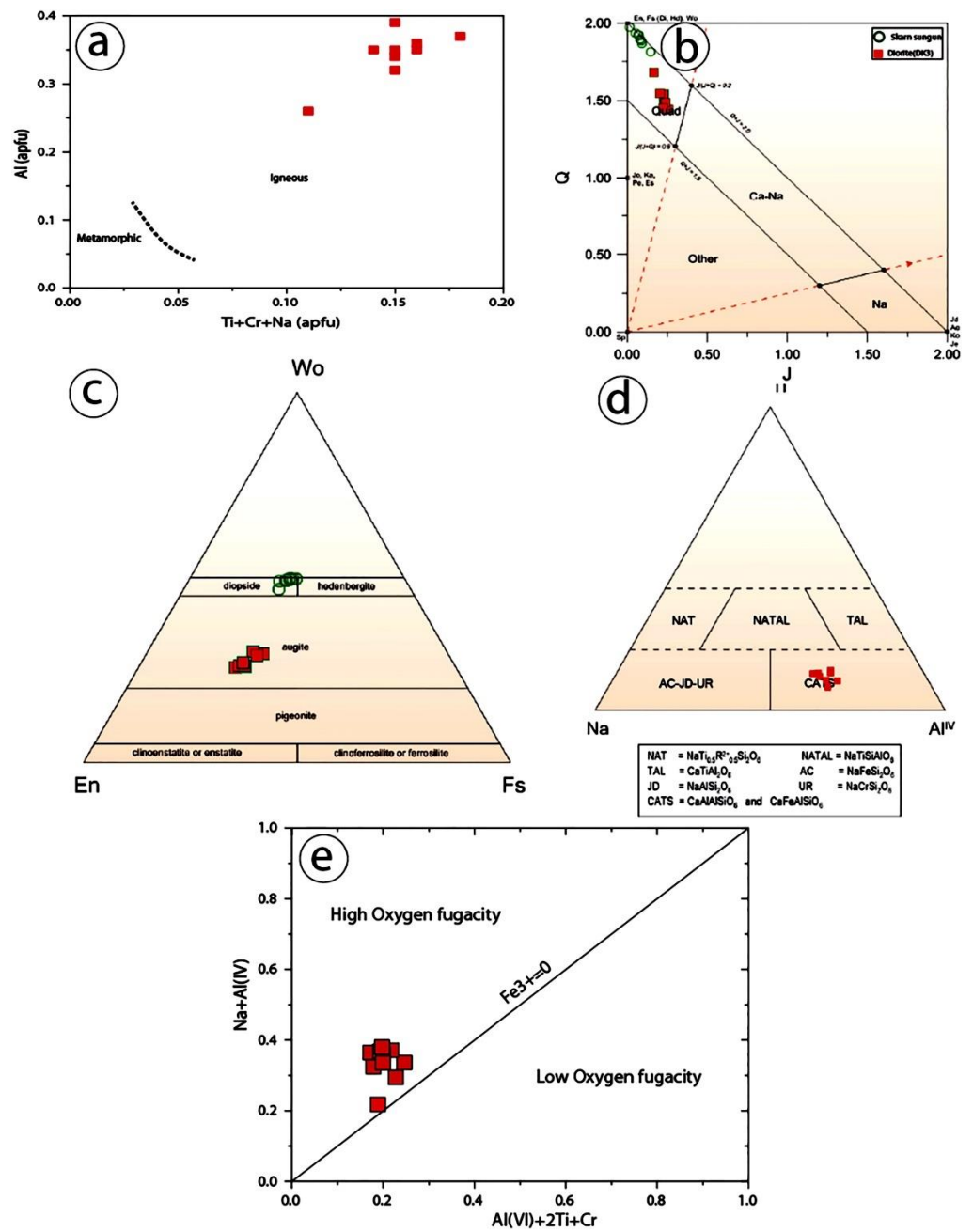
Figure 9. (**a**) Al diagram vs. Ti-Na- Cr to distinguish igneous from metamorphic pyroxene; all clinopyroxenes are located in igneous field [29]. (**b**) The Q-J clinopyroxene classification diagram [27]. (**c**) Wo-En-Fs ternary diagrams of pyroxene [27]. (**d**) Clinopyroxene ternary diagram of Ti-Na- Al^{IV}, studied samples are located exclusively in the CATS field. (e) An estimation of oxygen fugacity from pyroxene crystals compositions in diorite dykes [30].

Oxygen fugacity has a special effect on changes in the liquidus temperature and magma composition [31] and is also an effective factor for controlling magmatic processes and the sequence of crystallization [32–35]. To determine the degree of oxygen fugacity in the primary magma by using clinopyroxene, the total amount of $Al^{IV} + 2Ti + Cr$ was used against $Na + Al^{IV}$ [30] (Figure 9e). Fe^{3+} in the octahedral position replaces elements, such as Cr and Al^{IV}. Therefore, the clinopyroxene amount of Fe^{3+} in pyroxenes depends strongly on the amount of Al^{IV}: whenever more aluminum enters into the tetrahedral position, the possibility for Fe^{3+} to enter M sites will increase. In the diagram (Figure 9e), the $Fe^{3+} = 0$ line is a proxy for oxygen fugacity; data points that plot above the line indicate

high fugacities and distance from this line indicates greater fugacity values. Fe^{3+} content from Sungun is, thus, consistent with high oxygen fugacity during magmatic clinopyroxene crystallization.

7. Magmatic Series and Tectonic Environment

7.1. Magma Series from Amphibole Composition

Bivariate diagrams of Al_2O_3 vs. TiO_2 [36] are used to determine the source and nature of the magma in diorite enclaves in the region from the chemical composition of amphibole. Studied samples are largely located within the sub-alkaline field, with only a few transitional samples plotting within the sub-alkaline and alkaline field (Figure 10a,b). These data are consistent with previously reported whole-rock geochemistry showing the calc-alkalic to alkalic nature of the Sungun magmas [18].
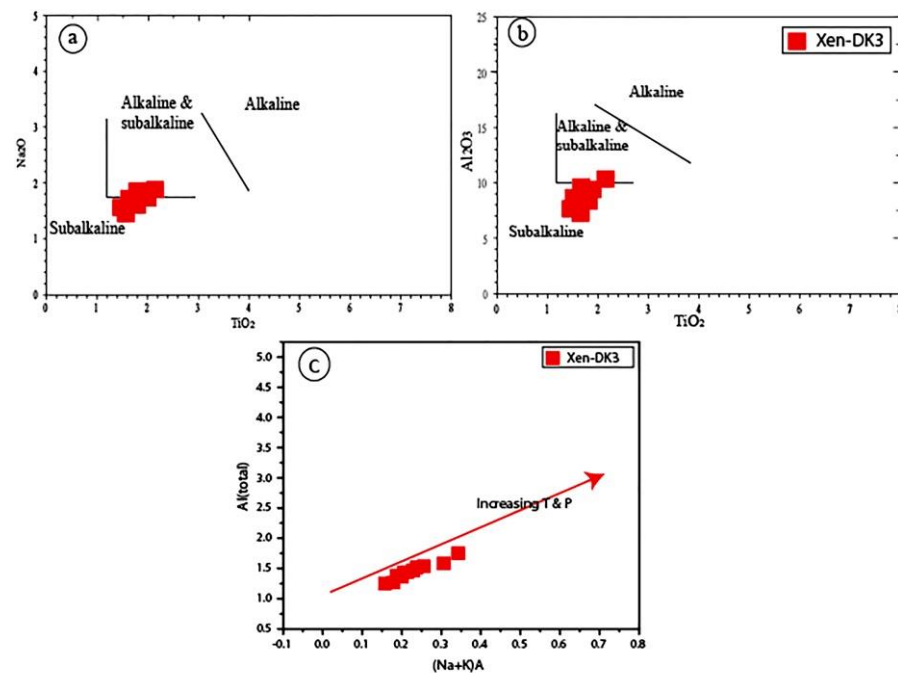
Figure 10. (**a**) Al_2O_3 vs. TiO_2 and (**b**) Na_2O vs. TiO_2 diagram for amphibole [36]. The dioritic enclave samples are dominantly located in subalkaline fields. (**c**) (Na+K) A vs. (Al) total in amphiboles and diorite enclaves.

7.2. Temperature Estimates from Chlorite

Temperatures estimated from Sungun chlorite compositions are provided in Table 5 for several chlorite geothermometers [37–41]. The estimates obtained from models by [37,40] are most applicable to diagenetic, hydrothermal and metamorphic environments because the tetrahedral structure of aluminum is independent from bulk rock chemistry:

$$T \, (^{\circ}C) = -61.92 + 321.98 Al^{IV} \tag{1}$$

The authors of [40] categorized geo-thermometers for chlorite formed in hydrothermal environments saturated in aluminum (i.e., in the presence of other aluminum minerals). They corrected the tetrahedral structure of aluminum and rewrote Equation (1):

$$Alc^{IV} = Al^{IV} + 0.7 Fe/(Fe + Mg) T = 106 Alc^{IV} + 18 \tag{2}$$

The correction to Equation (2) proposed by [41], which is applicable to similar temperature ranges, is only applicable for low-Fe chlorite (Fe > 0.6). The [40] model is, thus, the most appropriate for this study.

The authors of [42] studied combinations of chlorite in the meta-volcanic rocks of the Barton Greenstone belt, which includes basalt and dacite, and they proposed a chlorite geo-thermometer equation with a correction of 0.31 for the Fe/(Fe+Mg) ratio:

$$TX97\text{-}Al^{IV} \ (°C) = 106.99 \times ((Al^{IV}O28) + 1.33 \times (0.31 - Fe/(Fe+Mg))) - 61.92 \text{ if } Fe/((Fe + Mg)) < 0.31 \tag{3}$$

$$TX97\text{-}Al^{IV} \ (°C) = 106.99 \times ((Al^{IV}O28) + 1.33 \times (0.31 - Fe/(Fe + Mg))) - 61.92 \text{ if } Fe/((Fe+Mg)) > 0.31 \tag{4}$$

Several experimental correction factors were used in chlorite geo-thermometers to reduce the effect of bulk rock composition and contamination from other aluminum phases (e.g., [37,43]). For most experimental chlorite geo-thermometers, the amount of Al^{IV} is estimated by using the 28-oxygen normalization method; however, in other models, a normalization to 14-oxygen is preferred. Nevertheless, the application of both chlorite normalizations (i.e., differences in sites of octahedral occupation) to the same geo-thermometer generates only minor variations in modeled temperatures.

Results from the two favored chlorite geothermometers ([37,40] Table 5) indicate temperatures ranging between 263 °C and 311 °C for DK1b diorite enclaves and between 230 °C and 258 °C for DK3 microdiorite enclaves.

Table 5. Results of the thermometry calculations of chlorites in the diorite and microdiorite enclaves.

Sample		[37]	[40]	[43]	[39]	[38]	[44]	[41]	[45]	[42]	[46]
b1		271	319	328	241	337	280	305	251	206	231
b2		255	303	305	209	313	244	285	237	188	217
b3		258	306	309	214	317	249	289	238	188	218
b4		260	309	312	219	321	255	298	240	188	220
b5	DK1b	260	309	313	219	321	255	291	240	189	220
b6		265	313	320	229	328	267	292	246	201	226
b7		272	320	330	244	338	282	306	253	211	233
b8		244	291	289	189	297	218	282	227	177	207
b9		268	316	325	237	333	274	296	250	206	229
b10		273	322	332	248	341	286	295	253	209	233
Average		263	311	316	225	325	261	294	244	196	223
Max		273	322	332	248	341	286	306	253	211	233
Min		244	291	289	189	297	218	282	227	177	207
k1		229	257	266	165	266	183	248	237	267	219
k2		232	259	270	169	270	189	252	239	270	221
k3		228	255	264	163	264	180	246	236	267	218
k4		233	260	271	170	271	191	258	240	271	222
k5		238	266	279	178	279	203	267	245	277	227
k6		229	256	265	164	265	182	256	236	266	219
k7		226	253	260	160	260	174	257	233	262	215
k8	DK3	230	257	267	166	267	185	264	238	270	220
k9		235	263	274	173	274	195	266	241	272	224
k10		225	252	259	158	258	172	252	232	260	214
k11		231	258	268	167	268	187	261	238	269	221
k12		222	249	255	155	255	166	249	231	261	213
k13		222	248	254	154	254	165	258	230	260	212
k14		240	267	282	182	282	208	275	247	282	229
k15		237	265	277	176	277	200	264	244	276	226
Average		230	258	267	167	267	185	258	238	269	220
Max		240	267	282	182	282	208	275	247	282	229
Min		222	248	254	154	254	165	246	230	260	212

7.3. Pressure and Temperature Estimates from Amphibole

Experimental results show that the composition of amphibole depends on pressure, temperature, oxygen partial pressure (fugacity), total composition of the rock and coeval formation of other mineral phases [47,48]. In this study, to estimate of crystallization pressure of selected amphiboles, four conventional methods were used based on Al in hornblende [48–51]; results are presented in Table 6. Pressure estimates obtained from these models range between 3.0 and 5.3 kilobars (approximate depths of 9 to 16 kilometers) and standard deviations generally indicate that the degree of variation for each of these methods is negligible.

Table 6. Results of geothermobarometery and oxygen fugacity from amphibole in the diorite enclaves (DK3).

Sample	P1 (kbar)	P2 (kbar)	P3 (kbar)	P4 (kbar)	T1 (oC)	T2 (oC)	T3 (oC)	T4 (oC)	fO2
X1	4.815	5.034	3.886	5.256	754	750	768	747	−13.63
X2	3.559	3.627	2.83	4.068	732	731	743	725	−14.67
X3	3.452	3.506	2.74	3.966	732	732	743	725	−14.75
X4	2.572	2.519	1.999	3.133	708	709	716	700	−15.51
X5	2.427	2.357	1.878	2.997	715	716	723	707	−15.64
X6	3.851	3.953	3.075	4.344	739	737	750	732	−14.42
X7	3.562	3.629	2.832	4.07	727	727	738	720	−14.67
X8	3.106	3.118	2.448	3.638	720	720	729	712	−15.05
X9	4.007	4.128	3.206	4.491	729	727	741	722	−14.28
X10	3.279	3.312	2.594	3.803	721	721	731	714	−14.91
Average	3.463	3.5183	2.7488	3.9766	727.7	727	738.2	720.4	−14.753
Max	4.815	5.034	3.886	5.256	754	750	768	747	−13.63
Min	2.427	2.357	1.878	2.997	708	709	716	700	−15.64

P1 = −3.92 + 5.03 * Al(total) [47]; P2 = −4.76 + 5.64 * Al(total) [48]; P3 = −3.46 + 4.23 * Al(total) [49]; p4 = −3.01 + 4.76 * Al(total) [50].

In all of the above models, the pressure of formation is determined solely from the total amount of Al and other parameters, such as temperature, are not considered. Many formulae have been proposed for calculating pressure. The model by [52] is appropriate for conditions consistent with convergent margins:

$$P \text{ (kbar)} = -3.01 + 4.76(\text{Al total}) \tag{5}$$

The above formula allows for the determination of peak pressures of crystallization [51]. High amounts of magnetite and ilmenite indicate high oxygen fugacity and the amphiboles that crystallize in such conditions tend to show more reliable results for geothermobarometry [47,48]. Plagioclase and hornblende grains that are adjacent and equilibrated with each other are useful for thermometry and the usage of this pair of minerals in igneous rocks is independent to the presence or absence of quartz.

The calculation of the temperature in the formula presented by [53] (Table 6) shows that the temperature range for the diorite enclaves is between 714 and 731 °C. This temperature indicates mineral replacement in diorite enclaves occurs within Dk3 diorite dykes during late magmatic stages. Diagrams of the main elements of amphibole compared to (Na + K)A and total aluminum Al (total), which, respectively, show the temperature [54] and pressure [48] conditions of amphibole crystallization, provide insight on the pressure and temperature conditions at the time of crystallization. Experimental studies have shown that atomic amounts of Al (total) and (Na + K)A depend on the temperature of the system and often exhibit high positive correlation with each other [55,56]. Analysis of these diagrams shows a positive correlation between amounts of Al(total) and (Na + K)A, consistent with such temperature increases for the dioritic enclaves (Figure 10c). According to these diagrams, amounts of Mg and Si decrease with increasing Al total. Decreases in Si are accompanied by increases in Ti (Figure 11), indicating substitution associated with

increasing pressure. With respect to (Na + K)A, negative correlations with Si and Mg are consistent with increasing temperatures (Figure 11). Mg decreases are likely related to replacement by Fe.
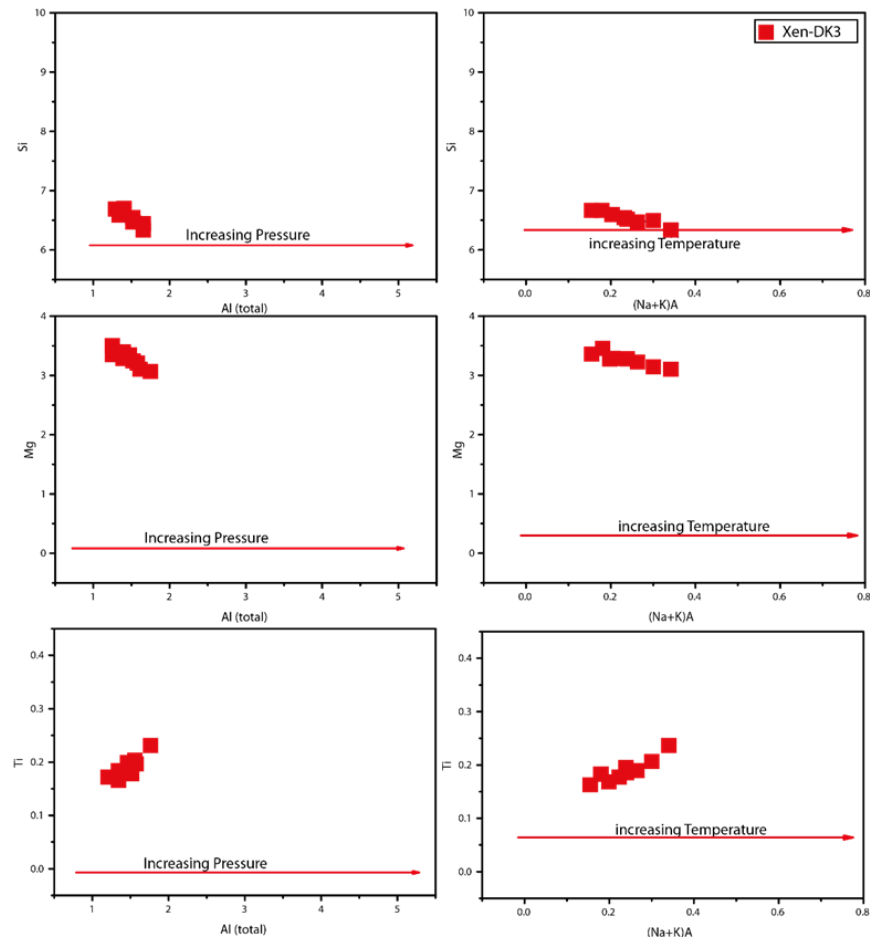
Figure 11. The Al (total) vs. Ti, Mg, Si and (Na+K) A diagram vs. the Ti, Mg, Si for the study of chemical composition changes in dioritic enclaves. Associated inferred pressure and temperature changes are indicated with red arrows.

7.4. Pressure and Temperature Estimates from Pyroxene

The Winpyrox application by [57] was used for the thermobarometric analysis of pyroxene. The chemical composition of pyroxenes is an important index for measuring temperature and pressure in igneous rocks. Experiential research shows that the amount of Al^{IV} in clinopyroxene depends on pressure [58]. The authors of [59] proposed a model for the estimation of temperature and pressure of clinopyroxene formation based on XPT and YPT indexes, which can be calculated with the following equations:

$$XpT = 0.446\, SiO_2 + 0.187\, TiO_2\; 0.404\, Al_2O_3 + 0.346\, FeO\,(tot)\; 0.052\, MnO + 0.309\, MgO + 0.431\, CaO\; 0.446\, Na_2O \qquad (6)$$

$$YpT = 0.369\, SiO_2 + 0.535\, TiO_2\; 0.317\;_{Al_2O_3} + 0.323\, FeO\,(tot) + 0.235\, MnO\; 0.516\, MgO - 0.167\, CaO\; 0.153\, Na_2O \qquad (7)$$

Using these indexes, we estimate pressures ranging between 11 and 15 kbar for the Sungun clinopyroxene (Figure 12a) and a temperature of formation ranging between 1250 °C and 1300 °C (Figure 12b). These are consistent with results from other geothermometers and geobarometers provided in Tables 7 and 8.
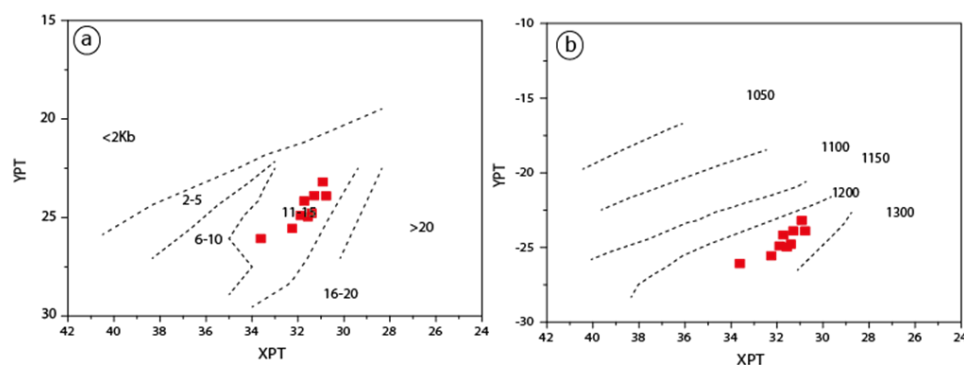
Figure 12. Estimations of (**a**) crystallization pressure and (**b**) crystallization temperature of clinopyroxene.

Table 7. Results of geobarometry calculations for clinopyroxene.

Rock Type	Sample No.	[60]	[61]	[62]	[63]
Error	Kbar	± 1.75	± 1.70	± 1.00	± 2.80
	1	13.72	14.66	16.01	17.87
	2	14.82	15.73	22.86	19.07
	3	13.64	14.41	24.53	19.49
	4	12.22	12.89	24.09	18.13
DK3	5	11.56	12.58	24.48	16.38
	6	13.21	14.11	25.20	18.25
	7	12.90	13.84	25.36	18.24
	8	13.44	14.35	25.66	18.16
	9	12.40	13.25	25.11	16.96
	10	13.76	14.54	25.38	18.09
	Max	14.82	15.73	25.66	19.49
	Min	11.56	12.58	16.01	16.38
	Average	13.17	14.06	23.36	18.04

Table 8. Results of the geothermometry calculations for clinopyroxene.

Rock Type	Sample No.	[64]	[65]	[66]	[66]	[67]
Error	°C	±50	±30	±30	±30	±30
	1	1431.00	1104.00	1172.00	816.00	894.00
	2	1425.00	1068.00	1171.00	854.00	901.00
	3	1427.00	1054.00	1178.00	867.00	903.00
	4	1419.00	1069.00	1185.00	863.00	902.00
DK3	5	1446.00	1170.00	1176.00	716.00	882.00
	6	1446.00	1125.00	1204.00	833.00	896.00
	7	1446.00	1136.00	1197.00	809.00	892.00
	8	1446.00	1113.00	1194.00	831.00	896.00
	9	1440.00	1119.00	1185.00	812.00	893.00
	10	1427.00	1083.00	1196.00	865.00	903.00
	Max	1446.00	1170.00	1204.00	867.00	903.00
	Min	1419.00	1054.00	1171.00	716.00	882.00
	Average	1434.83	1105.42	1186.08	820.75	895.58

8. Discussion and Conclusions

Previous studies on samples of Sungun dykes and Sungun porphyry show that they have bulk rock compositions more consistent with the post-collisional magmatic arc domain than magmas from continental active margins [4,11]. Similarities between REE patterns of

the dykes and the porphyry suggest that their magmas share a common origin. However, the dykes are compositionally slightly more mafic and younger in age. All samples, with the exception of the micro-diorite and lamprophyric, plot in similar $^{87}Sr/^{86}Sr$ versus $^{143}Nd/^{144}Nd$ space, showing ratios consistent with a mantle source [4]. The isotope ratio of these rocks originated mainly from the melt extraction from a mantle source within a closed system. Thermobarometry of the dykes indicates that their magmas formed from the extraction of an intermediate magma and another magma of mixed crustal-mantle affinity. At a maximum pressure of 19 kbar, gravitational separation of the magmas within a lower-crustal magmatic chamber gave rise to the dioritic magma. This magma then rose and settled into another chamber at a maximum of 6 kbar (~18 km), where it fractionated and gravitationally separated. These magmas rose again in sequence, thereby creating the more felsic and earlier Sungun porphyry and the subsequent more mafic Sungun dykes [16,18].

Dioritic dykes in the eastern skarn part of the Sungun copper deposit contain abundant clinopyroxene. Although previous workers proposed that these were inherited from the skarn [26], our work shows that the crystals are augitic, contrasting with the diopsidic composition of clinopyroxene from the skarn. We propose that they are magmatic in origin. Substitution mechanisms of studied clinopyroxenes depend on variations in physical and chemical conditions and the distribution of Al and Ti minerals in the source magma. Pressures of formation of clinopyroxene in diorite dykes are estimated between 11 and 15 kilobars and temperatures of 1200 °C, consistent with early stage, lower-crustal (maximum 19 kbar) magmatic activities deduced from dyke thermobarometry [11]. High Fe^{3+} contents are consistent with high oxygen fugacities during early magmatic conditions.

Results stemming from the mineral analyses of enclaves described in this work constrain the later-stage cooling and retrograde alteration processes that occurred in Sungun magmas. Amphibole crystallization occurred at fairly well-constrained temperatures (714–731 °C), at pressures ranging between 3.0 and 5.3 kbar (9–16 km), as later dioritic magmas rose upwards in the crust. Amphiboles within the enclaves consist of calcic amphibole and a sub-group of magnesio-hornblende; such compositions, along with high-cationic Fe, reflect high oxygen fugacity at the time of crystallization and are, thus, consistent with a supra-subduction-zone (magmatic arc) environment. As the system cooled, later hydrothermal alteration and chloritization occurred at much lower temperatures: the retrograde formation of chlorite in microdiorite and diorite occurred at approximately 272 °C and 257 °C, respectively.

Recent petrologic studies on intrusive rocks in the Sungun Cu-Mo porphyry deposit show that the main stock of the intrusion and its peripheral dykes consist of, in order of abundance, quartz monzonite, quartz diorite, gabbro diorite, microdiorite, dacite and lamprophyre [11]. Generally, enclaves observed in late dykes consist of quartz diorite, diorite, hornfels and microdiorite. These findings have implications for our understanding of the genesis of the intrusion and its deposit. Indeed, previous work has documented that the stock consists of an early quartz monzonitic magma pulse, followed by a dioritic/granodioritic pulse [13]. In contrast, our results suggest that the intrusion consists of multiple pulses expressed as several sequential episodes of magma intrusion that are more lithologically diverse than previously described. Furthermore, the temperature of chloritization documented here is consistent but at the lower temperature range of previous estimates for propylitic hydrothermal alteration at Sungun [8].

References

1. Sillitoe, R.H. Porphyry copper systems. *Econ. Geol.* **2010**, *105*, 3–41. [CrossRef]
2. Richards, J.P. Postsubduction porphyry Cu-Au and epithermal Au deposits: Products of remelting of subduction-modified lithosphere. *Geology* **2009**, *37*, 247–250. [CrossRef]
3. Logan, J.M.; Mihalynuk, M.G. Tectonic controls on early Mesozoic paired alkaline porphyry deposit belts (Cu-Au ± Ag-Pt-Pd-Mo) within the Canadian Cordillera. *Econ. Geol.* **2014**, *109*, 827–858. [CrossRef]
4. Kamali, A.A.; Moayyed, M.; Amel, N.; Hosseinzadeh, M.R.; Mohammadiha, K.; Santos, J.F.; Brenna, M. Post-mineralization, cogenetic magmatism at the sungun cu-mo porphyry deposit (Northwest Iran): Protracted melting and extraction in an arc system. *Minerals* **2018**, *8*, 588. [CrossRef]
5. Nabavi, M.H. *An Introduction to the Geology of Iran*; Geological Survey of Iran: Tehran, Iran, 1976.
6. Moayyed, M. Petrologic Studies of Tertiary Volcano-Plutonic Belt in Western Alborz-Azerbaijan, with a Special Focus on Hashtchin Area, Iran. Ph.D. Thesis, University of Shahid Beheshti, Tehran, Iran, 2001.
7. Osanloo, M.; Ataei, M. Using 2d lerchs and grossmann algorithm to design final pit limits of sungun copper deposit of Iran. *Int. J. Eng.* **2000**, *13*, 81–89.
8. Hezarkhani, A.; Williams-Jones, A.E. Controls of alteration and mineralization in the Sungun porphyry copper deposit, Iran; evidence from fluid inclusions and stable isotopes. *Econ. Geol.* **1998**, *93*, 651–670. [CrossRef]
9. Hassanpour, S. Metallogeny and Mineralization of Copper and Gold in Arasbaran Zone (Eastern Azerbaijan). Ph.D. Thesis, Shahid Beheshti University, Tehran, Iran, 2010. (In Persian with English Abstract).
10. Jamali, H.; Dilek, Y.; Daliran, F.; Yaghubpur, A.; Mehrabi, B. Metallogeny and tectonic evolution of the Cenozoic Ahar—Arasbaran volcanic belt, northern Iran. *Int. Geol. Rev.* **2010**, *52*, 608–630. [CrossRef]
11. Kamali, A.A.; Moayyed, M.; Amel, N.; Mohammad, F.; Brenna, M.; Saumur, B.M.; Santos, J.F.J.F. Mineralogy, mineral chemistry and thermobarometry of post-mineralization dykes of the Sungun Cu–Mo porphyry deposit (Northwest Iran). *Open Geosci.* **2020**, *12*, 764–790. [CrossRef]
12. Richards, J.P.; Wilkinson, D.; Ullrich, T. Geology of the Sari Gunay Epithermal Gold Deposit, Northwest Iran. *Econ. Geol.* **2006**, *101*, 1455–1496. [CrossRef]
13. Hezarkhani, A. Petrology of the intrusive rocks within the Sungun porphyry copper deposit, Azerbaijan, Iran. *J. Asian Earth Sci.* **2006**, *27*, 326–340. [CrossRef]
14. Kamali, A.; Moayyed, M.; Amel, N.; Hosainzadeh, M.R. Mineral chemistry and geochemistry of lamprophyric dykes in the Sungun Cu-Mo porphyry deposit (Varzaghan-Northwestern Iran). *J. Geosci.* **2017**, *26*, 73–90.
15. Aghazadeh, M.; Hou, Z.; Badrzadeh, Z.; Zhou, L. Temporal–spatial distribution and tectonic setting of porphyry copper deposits in Iran: Constraints from zircon U–Pb and molybdenite Re–Os geochronology. *Ore Geol. Rev.* **2015**, *70*, 385–406. [CrossRef]
16. Mehrpartou, M. Contributions to the Geology, Geochemistry, Ore Genesis and Fluid Inclusion Investigations on Sungun Cu-Mo Porphyry Deposit (North-West of Iran). Ph.D. Thesis, Hamburg University, Hamburg, Germany, 1993.
17. Kamali, A.; Moayyed, M.; Amel, N.; Hosseinzadeh, M.R. Mineralogy and Mineral Chemistry of Quartz-Dioritic Dykes of Sungun Mo- Cu Porphyry Deposit (NW Iran). *Iran. J. Crystallogr. Mineral.* **2017**, *25*, 123–138.
18. Kamali, A.A. Petrology and Mineral Chemistry of Post Mineralization Dykes of Sungun Cu-Mo Porphyry Deposit, North of Varzegan, East-Azerbaijan. Ph.D. Thesis, University of Tabriz, Tabriz, Iran, 2016.
19. Deer, W.A.; Howie, R.A.; Zussman, J. *An Introduction to the Rock-Forming Minerals*, 2nd ed.; Pearson: London, UK, 1992, ISBN 0582300940.
20. Moazen, M. Chlorite-Chloritoid-Garnet Equilibria and Geothermometry in the Sanandaj-Sirjan Me-Tamorphic Belt, Southern Iran. *Iran. J. Sci. Technol. Trans. A Sci.* **2004**, *28*, 65–78.
21. Chabu, M. The geochemistry of phlogopite and chlorite from the Kipushi Zn-Pb-Cu deposit, Shaba, Zaire. *Can. Mineral.* **1995**, *33*, 547–558.
22. Leake, B.E.; Woolley, A.R.; Arps, C.E.S.; Birch, W.D.; Gilbert, M.C.; Grice, J.D.; Hawthorne, F.C.; Kato, A.; Kisch, H.J.; Krivovichev, V.G. Report. Nomenclature of amphiboles: Report of the subcommittee on amphiboles of the international mineralogical association commission on new minerals and mineral names. *Mineral. Mag.* **1997**, *61*, 295–321. [CrossRef]
23. Anderson, J.L.; Smith, D.R. The effects of temperature and f_{O2} on the Al-in-hornblende barometer. *Am. Mineral.* **1995**, *80*, 549–559. [CrossRef]
24. Speer, J.A. Micas in Igneous Rocks. *Rev. Mineral. Geochemistry* **1984**, *13*, 299–356.
25. Wones, D.R. Significance of the Assemblage Titanite+ Magnetite+ Quartz in Granitic Rocks. *Am. Mineral.* **1989**, *74*, 744–749.
26. Alavi, G. Study of the skarn deposits around the Sheyvar-Dagh batolith and comparison with the Sungun porphyry skarn. *Geology. Tabriz* **2014**.
27. Morimoto, N. Nomenclature of pyroxenes. *Mineral. J.* **1989**, *14*, 198–221. [CrossRef]

28. Papike, J.J. Amphiboles and pyroxenes: Characterization of other than quadrilateral components estimates of ferric iron from microprobe data. *Geol. Soc. Am. Abstr. Programs* **1974**, *6*, 1053–1054.

29. Berger, J.; Femenias, O.; Mercier, J.C.C.; Demaiffe, D. Ocean-floor hydrothermal metamorphism in the Limousin ophiolites (western French Massif Central): Evidence of a rare preserved Variscan oceanic marker. *J. Metamorph. Geol.* **2005**, *23*, 795–812. [CrossRef]

30. Schweitzer, E.L.; Papike, J.J.; Bence, A.E. Statistical analysis of clinopyroxenes from deep-sea basalts. *Am. Mineral.* **1979**, *64*, 501–513. [CrossRef]

31. France, L.; Ildefonse, B.; Koepke, J.; Bech, F. A new method to estimate the oxidation state of basaltic series from microprobe analyses. *J. Volcanol. Geotherm. Res.* **2010**, *189*, 340–346. [CrossRef]

32. Botcharnikov, R.E.; Koepke, J.; Holtz, F.; McCammon, C.; Wilke, M. The effect of water activity on the oxidation and structural state of Fe in a ferro-basaltic melt. *Geochim. Cosmochim. Acta* **2005**, *69*, 5071–5085. [CrossRef]

33. Kilinc, A.; Carmichael, I.S.E.E.; Rivers, M.L.; Sack, R.O. The ferric-ferrous ratio of natural silicate liquids equilibrated in air. *Contrib. Mineral. Petrol.* **1983**, *83*, 136–140. [CrossRef]

34. Kress, V.C.; Carmichael, I.S.E.E. The compressibility of silicate liquids containing Fe_2O_3 and the effect of composition, temperature, oxygen fugacity and pressure on their redox states. *Contrib. Mineral. Petrol.* **1991**, *108*, 82–92. [CrossRef]

35. Moretti, R. Polymerisation, basicity, oxidation state and their role in ionic modelling of silicate melts. *Ann. Geophys.* **2005**, *48*, 583–608. [CrossRef]

36. Molina, J.F.; Scarrow, J.H.; Montero, P.G.; Bea, F. High-Ti amphibole as a petrogenetic indicator of magma chemistry: Evidence for mildly alkalic-hybrid melts during evolution of Variscan basic—Ultrabasic magmatism of Central Iberia. *Contrib. Mineral. Petrol.* **2009**, *158*, 69–98. [CrossRef]

37. Cathelineau, M.; Nieva, D. A chlorite solid solution geothermometer the Los Azufres (Mexico) geothermal system. *Contrib. Mineral. Petrol.* **1985**, *91*, 235–244. [CrossRef]

38. Jowett, E.C. Fitting iron and magnesium into the hydrothermal chlorite geothermometer. In Proceedings of the GAC/MAC/SEG Joint Annual Meeting, Toronto, ON, Canada, 27–29 May 1991. Program with Abstracts 16.

39. Kavalieris, I.; Walshe, J.L.; Halley, S.; Harrold, B.P. Dome-related gold mineralization in the Pani volcanic complex, North Sulawesi, Indonesia; a study of geologic relations, fluid inclusions, and chlorite compositions. *Econ. Geol.* **1990**, *85*, 1208–1225. [CrossRef]

40. Kranidiotis, P.; MacLean, W.H. Systematics of chlorite alteration at the Phelps Dodge massive sulfide deposit, Matagami, Quebec. *Econ. Geol.* **1987**, *82*, 1898–1911. [CrossRef]

41. De Caritat, P.; Hutcheon, I.A.N.; Walshe, J.L. Chlorite geothermometry: A review. *Clays Clay Miner.* **1993**, *41*, 219–239. [CrossRef]

42. Xie, X.; Byerly, G.R.; Ferrell, R.E., Jr. IIb trioctahedral chlorite from the Barberton greenstone belt: Crystal structure and rock composition constraints with implications to geothermometry. *Contrib. Mineral. Petrol.* **1997**, *126*, 275–291. [CrossRef]

43. Cathelineau, M. Cation site occupancy in chlorites and illites as function of temperature. *Clay Miner.* **1988**, *23*, 471–485. [CrossRef]

44. Hillier, S.; Velde, B. Octahedral Occupancy and the Chemical Composition of Diagenetic (Low-Temperature) Chlorites. *Clay Miner.* **1991**, *26*, 149–168. [CrossRef]

45. Zang, W.; Fyfe, W.S. Chloritization of the Hydrothermally Altered Bedrock at the Igarapé Bahia Gold Deposit, Carajás, Brazil. *Miner. Depos.* **1995**, *30*, 30–38. [CrossRef]

46. El-Sharkawy, M.F. Talc Mineralization of Ultramafic Affinity in the Eastern Desert of Egypt. *Miner. Depos.* **2000**, *35*, 346–363. [CrossRef]

47. Esawi, E.K. AMPH-CLASS: An Excel spreadsheet for the classification and nomenclature of amphiboles based on the 1997 recommendations of the International Mineralogical Association. *Comput. Geosci.* **2004**, *30*, 753–760. [CrossRef]

48. Hammarstrom, J.M.; Zen, E. Aluminum in hornblende: An empirical igneous geobarometer. *Am. Mineral.* **1986**, *71*, 1297–1313.

49. Hollister, L.S.; Grissom, G.C.; Peters, E.K.; Stowell, H.H.; Sisson, V.B. Confirmation of the empirical correlation of Al in hornblende with pressure of solidification of calc-alkaline plutons. *Am. Mineral.* **1987**, *72*, 231–239.

50. Johnson, M.C.; Rutherford, M.J. Experimental calibration of the aluminum-in-hornblende geobarometer with application to Long Valley caldera (California) volcanic rocks. *Geology* **1989**, *17*, 837–841. [CrossRef]

51. Schmidt, M.W. Amphibole composition in tonalite as a function of pressure: An experimental calibration of the Al-in-hornblende barometer. *Contrib. Mineral. Petrol.* **1992**, *110*, 304–310. [CrossRef]

52. lNonn Spnpn, J.A.; Vyhnal, C.R.; McSween, H.Y.; Speer, J.A. Hornblende chemistry in southern Appalachian granitoids: Implications for aluminum hornblende thermobarometry and magmatic epidote stability. *Am. Mineral.* **1991**, *76*, 176–188.

53. Blundy, J.D.; Holland, T.J.B. Calcic amphibole equilibria and a new amphibole-plagioclase geothermometer. *Contrib. Mineral. Petrol.* **1990**, *104*, 208–224. [CrossRef]

54. Humphreys, M.C.S.; Edmonds, M.; Christopher, T.; Hards, V. Chlorine variations in the magma of Soufrière Hills Volcano, Montserrat: Insights from Cl in hornblende and melt inclusions. *Geochim. Cosmochim. Acta* **2009**, *73*, 5693–5708. [CrossRef]

55. Rutherford, M.J.; Devine, J.D. Magmatic conditions and magma ascent as indicated by hornblende phase equilibria and reactions in the 1995–2002 Soufriere Hills magma. *J. Petrol.* **2003**, *44*, 1433–1453. [CrossRef]

56. Scaillet, B.; Evans, B.W. The 15 June 1991 Eruption of Mount Pinatubo. I. Phase Equilibria and Pre-eruption P-T-fO_2-fH_2O Conditions of the Dacite Magma. *J. Petrol.* **1999**, *40*, 381–411. [CrossRef]

57. Yavuz, F. WinPyrox: A Windows program for pyroxene calculation classification and thermobarometry. *Am. Mineral.* **2013**, *98*, 1338–1359. [CrossRef]

58. Thompson, R.N. Some high-pressure pyroxenes. *Mineral. Mag.* **1974**, *39*, 768–787. [CrossRef]

59. Soesoo, A. A multivariate statistical analysis of clinopyroxene composition: Empirical coordinates for the crystallisation PT-estimations. *GFF* **1997**, *119*, 55–60. [CrossRef]

60. Nimis, P. A Clinopyroxene Geobarometer for Basaltic Systems Based on Crystal-Structure Modeling. *Contrib. Mineral. Petrol.* **1995**, *121*, 115–125. [CrossRef]

61. Nimis, P.; Ulmer, P. Clinopyroxene Geobarometry of Magmatic Rocks Part 1: An Expanded Structural Geobarometer for Anhydrous and Hydrous, Basic and Ultrabasic Systems. *Contrib. Mineral. Petrol.* **1998**, *133*, 122–135. [CrossRef]

62. Nimis, P. Clinopyroxene Geobarometry of Magmatic Rocks. Part 2. Structural Geobarometers for Basic to Acid, Tholeiitic and Mildly Alkaline Magmatic Systems. *Contrib. Mineral. Petrol.* **1999**, *135*, 62–74. [CrossRef]

63. Putirka, K.D. Thermometers and Barometers for Volcanic Systems. *Rev. Mineral. Geochem.* **2008**, *69*, 61–120. [CrossRef]

64. Bertrand, P.; Mercier, J.-C.C. The Mutual Solubility of Coexisting Ortho- and Clinopyroxene: Toward an Absolute Geothermometer for the Natural System? *Earth Planet. Sci. Lett.* **1985**, *76*, 109–122. [CrossRef]

65. Nimis, P.; Taylor, W.R. Single Clinopyroxene Thermobarometry for Garnet Peridotites. Part I. Calibration and Testing of a Cr-in-Cpx Barometer and an Enstatite-in-Cpx Thermometer. *Contrib. Mineral. Petrol.* **2000**, *139*, 541–554. [CrossRef]

66. Negro, A.D.; Carbonin, S.; Salviulo, G.; Piccirillo, E.M.; Cundari, A. Crystal Chemistry and Site Configuration of the Clinopyroxene from Leucite-Bearing Rocks and Related Genetic Significance: The Sabatini Lavas, Roman Region, Italy. *J. Petrol.* **1985**, *26*, 1027–1040. [CrossRef]

67. Molina, G.; Zanazzi, P.F.; Mineralogy, P.Z.-E.J. Intracrystalline Fe^{2+} − Mg Ordering in Augite: Experimental Study and Geothermometric Applications. *Eur. J. Mineral.* **1991**, *3*, 863–876. [CrossRef]